Nano Today 58 (2024) 102449

Contents lists available at ScienceDirect

Nano Today

journal homepage: www.elsevier.com/locate/nanotoday

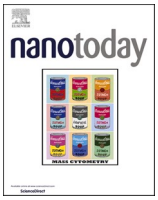

Programmed degradable core-shell nanoparticles eradicate mature biofilm via precise in-situ phototherapy

Fanqiang Bu [a], Mengnan Liu [a], Wangtao Zhao [a], Fang Liu [b], Wensheng Xie [a], Guofeng Li [a,*], Xing Wang [a,*]

[a] State Key Laboratory of Organic-Inorganic Composites, Beijing Laboratory of Biomedical Materials, Beijing University of Chemical Technology, Beijing 100029, PR China
[b] Department of Gastroenterology, China-Japan Friendship Hospital, Beijing 100029, PR China

ARTICLE INFO

Keywords:
Electroneutral nanoparticle
Programmed degradation of core-shell structure
Methicillin-resistant *Staphylococcus aureus* (MRSA) biofilm
Targeting bacteria within biofilm
In-situ phototherapy

ABSTRACT

Combating bacterial biofilm poses a significant challenge because of the dense extracellular polymeric substance (EPS) barrier and inherent drug tolerance. Herein, the designed core-shell nanoparticles (DA_3-NPs) that eradicate biofilm by precise *in-situ* phototherapy are reported. DA_3-NPs are self-assembled using thermosensitive azo-polymers (AP_3) to encapsulate GSH-degradable phototherapeutic polymers (DBP) *via* charge interaction. Notably, *D*-aminoalanine grafted onto the AP_3 serves as a critical component, providing an electroneutral shell and bacterial peptidoglycan targeting ability to the DA_3-NPs. Consequently, DA_3-NPs effectively penetrate EPS up to a depth of 60 μm and precisely target the bacteria within the biofilms. Upon exposure to laser irradiation and the GSH microenvironment, DA_3-NPs undergo sequential responses involving shell detachment and core disintegration. These processes facilitate point-to-point bacterial killing through the *in-situ* generations of ROS, carbon radicals and heat damage to the internal bacteria. Compared to non-targeted nanoparticles, DA_3-NPs exhibit a 61-fold increase in biofilm removal efficiency. This study thus presents a precise *in-situ* phototherapy strategy for nonantibiotic treatment of biofilm infections.

Introduction

Resistant bacteria and associated biofilm are the main cause of implant failure and chronic infection, which seriously threaten public health [1–3]. Biofilm possesses a dense extracellular polymeric substance (EPS) that greatly prevents immune cell killing and drug penetration [4,5]. Moreover, high concentrations of glutathione (GSH) in biofilm protect bacteria from oxidative stress, and the internal environmental pressure of biofilm enforce the bacteria to be in a low metabolic state [6,7]. These factors further attenuate the anti-bacterial efficacy of drugs. Therefore, the stubborn bacteria in biofilm are difficult to eradicate [8–10]. An ideal treatment strategy for biofilm removal requires effective biofilm penetration and internal bacteria killing.

Phototherapy, including photothermal therapy (PTT) and photodynamic therapy (PDT), employs phototherapy agents (PAs) to generate heat damage or reactive oxygen species (ROS) under light irradiation. It is a robust strategy for killing planktonic bacteria without inducing drug resistance [11–13]. However, phototherapy used for biofilm elimination has been limited. i) The dense EPS interferes with the penetration of PAs; ii) high-concentration GSH in biofilm consumes the ROS generated by phototherapy; and iii) bacteria that settle in different cubicles of biofilms can evade the killing of ROS and heat damage generated by the PAs [14–16]. These obstacles greatly weaken the efficacy of phototherapy, resulting in unsatisfactory anti-biofilm performances. Accordingly, targeted phototherapy is proposed as a promising approach to fight against these stubborn bacteria and the associated biofilm [17–19]. Particularly, targeted delivery of PAs *via* stimuli response (e.g. charge, pH, GSH, enzyme), in which tailored physicochemical techniques are used to trigger the targeted release and enrichment of PAs in the infection site depending on the unique microenvironment of biofilm, exhibits strong impact on reinforcing the efficacy of phototherapy [20–23]. Despite the very recent advances in designing targeted phototherapy, delivering PAs by stimuli-response is susceptible to microenvironment changes, resulting in off-target effects. As such, these delivery strategies are in favor of biofilm targeting rather than biofilm inhabitants (namely internal bacteria) targeting. To date, practical methods for precise and

* Corresponding authors.
E-mail addresses: ligf@mail.buct.edu.cn (G. Li), wangxing@mail.buct.edu.cn (X. Wang).

https://doi.org/10.1016/j.nantod.2024.102449
Received 22 May 2024; Received in revised form 20 July 2024; Accepted 11 August 2024
Available online 16 August 2024

accurate phototherapy targeting the biofilm inhabitants remain elusive. To achieve precise in-situ phototherapy, effective EPS penetration of PAs would be the crucial first step. It has been reported that magnetic actuation, optical actuation, catalytic effects, microneedle delivery, enzymatic degradation, and physicochemical modulation of nanoparticle structures are conducive to boosting EPS penetration [24–29]. Additionally, targeting biofilm inhabitants is enabled for the point-to-point killing of the internal bacteria, while the relief of the environmental pressure in the biofilm maximizes the efficacy of phototherapy. Thus, such an approach could offer optimal phototherapy efficacy against resistant bacteria and associated biofilm.

Here, a unique core-shell shaped nanoparticles (DA_3-NPs) that possessed a robust capacity of precise *in-situ* phototherapy for eradicating Methicillin-resistant *Staphylococcus aureus* (MRSA) associated biofilm was proposed (Scheme 1). First, a GSH degradable pseudo semiconducting polymer (DBP), which generated ROS and heat damage under laser irradiation, was synthesized. Then, DBP was encapsulated in an amphiphilic thermosensitive polyester (AP_3) shell by the perfectly matched charge interaction to obtain DA_3-NPs. In particular, *D*-aminoalanine in AP_3 was used as a critical molecule to provide DA_3-NPs with an electroneutral shell that functioned bacterial targeting ability. Once coming into contact with a biofilm, the electroneutral DA_3-NPs were able to penetrate and diffuse within the biofilm matrix, rather than interacting with the EPS substances. Subsequently, DA_3-NPs targeted the bacteria enclosed within the biofilm *via* specific peptidoglycan insertion of the *D*-aminoalanine functional groups [30]. Under laser irradiation, the azo bonds of the shell structure in DA_3-NPs could be broken by the generated heat, resulting in the detachment of the AP_3 shell and exposure of the DBP core. The disulfide bonds in the DBP core were then broken when contacted with GSH, triggering the responses of core disintegration in a sequential manner. As such, the DA_3-NPs could generate ROS, carbon radicals and heat damage precisely in the bacterial residence and notably enhanced the anti-biofilm efficacy. Moreover, carbon radicals production and GSH consumption in these processes further augmented the performance of DA_3-NPs, while these treatment processes could activate the immune response for biofilm elimination by polarizing macrophages into an M2 phenotype. Consequently, DA_3-NPs significantly performed 61 times superior efficiency of mature biofilm removal compared with the non-targeted electronegative nanoparticles. Therefore, this study provides a potential strategy of *in-situ* phototherapy for treating biofilm infections.

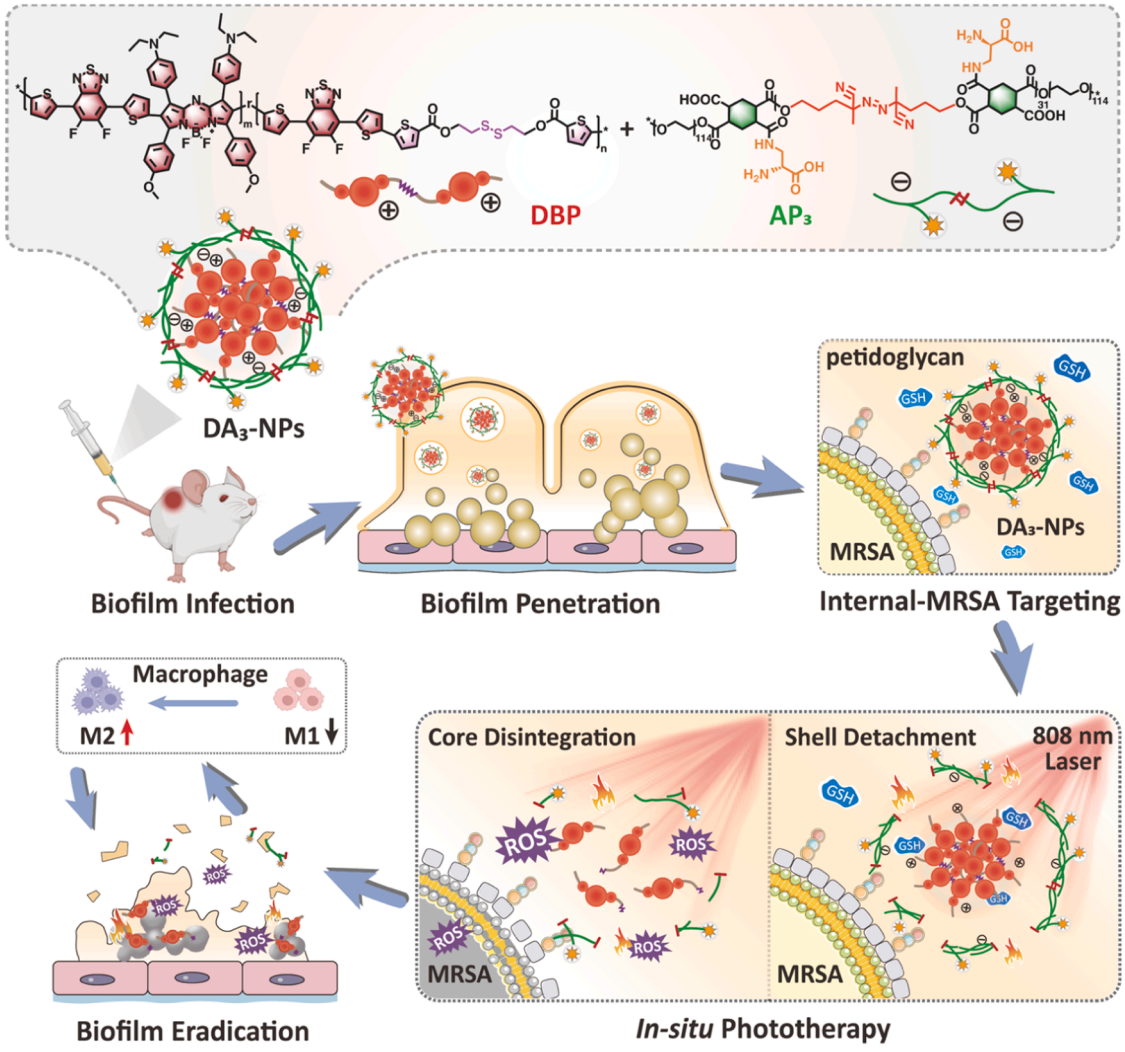

Scheme 1. Schematic representation of MRSA biofilm eradication by *in-situ* phototherapy of DA_3-NPs. Chemical structures of DBP and AP_3 and the assembled DA_3-NPs. Anti-biofilm mechanisms of DA_3-NPs involved in: EPS penetration, internal MRSA targeting, *in-situ* phototherapy, immune response modulation, and biofilm eradication.

Methods

Materials

5,6-difluoro-4,7-bis (5-(trimethylstannyl) thiophen-2-yl) benzo [c] [1,2,5] thiadiazole, 1,2,4,5-cyclo hexanetetracarboxylic dianhydride, Polyethylene glycol-5 K (mPEG5K-OH), 1,2- Benzenedicarboxaldehyde (OPA), glutathione (GSH), and 4,4′-Azobis(4-cyano-1-pentanol) were purchased from InnoChem Science & Technology Co., Ltd (Beijing, China). 2,2,6,6-tetramethylpiperidine (TEMP), 1,3-Diphenylisobenzofuran (DPBF), 2,2'-azino-bis(3-ethylbenzothiazoline-6-sulfonic acid) (ABTS), crystal violet (CV), fluorescein isothiocyanate (FITC), Nile Red, dimethylaminoazobenzene oxide (DDAO), 4′,6-diamidino-2-phenylindole (DAPI), 2′,7′-dichlorodihydrofluorescein diacetate (DCFH-DA), and propidium iodide (PI) were purchased from Solarbio (Beijing, China). Bacterial viability kit (Invitrogen LIVE/DEAD BacLight, L13152), bacterial membrane permeability, protein leakage, and ATPase activity ELISA kit was purchased from Thermo Fisher (Beijing, China). F4/80 antibody, CD80 antibody, and CD206 antibody were purchased from Biolegend (U.S.A.). All reagents purchased from Aladdin (Shanghai, China).

Synthesis of S1 monomer

According to literature reports, the S1 precursor compound was synthesized [31]. ^{1}H NMR (400 MHz, DMSO-d_6) δ 8.09 (dd, 4 H), 7.20 (s, 1 H), 7.09 (d, 2 H), 6.82 (d, 2 H), 3.87 (s, 3 H), 3.48 (q, 4 H), 1.18 (t, 6 H). The S1 precursor compound (2 mmol, 1338.7 mg) and *N*-Bromosuccinimide (NBS, 5 mmol, 899.9 mg) were added to 20 mL dichloromethane (DCM). After reaction 12 h at room temperature, the mixture was obtained after rotary evaporation. The S1 was separated by column chromatography (DCM/petroleum ether (PE)=1/5). ^{1}H NMR (400 MHz, DMSO-d_6) δ 7.94 (d, 2 H), 7.60 (d, 2 H), 7.05 (d, 2 H), 6.87 (d, 2 H), 4.12 (m, 3 H), 3.83 (s, 4 H), 1.16 (t, 6 H).

Synthesis of S3 monomer

The 5-bromothiophene-2-carboxylic acid (33.30 mmol, 6.85 g), 1,4-butanediol (11.10 mmol, 1.00 g), 1-(3-Dimethylaminopropyl)-3-ethylcarbodiimide hydrochloride (EDC, 33.30 mmol, 6.38 g) and 4-Dimethylaminopyridine (DMAP, 33.30 mmol, 4.06 g) were added to 50 mL *N, N*-Dimethylformamide (DMF). The mixed solution was allowed to react for 2 h under N_2 protection. Then, the mixed solution was quenched with deionized water and further extracted with ethyl acetate (EA). The S3 was separated by column chromatography (DCM/EA = 5/1). ^{1}H NMR (400 MHz, DMSO-d_6) δ ppm 7.65 (d, 1 H), 7.38 (d, 1 H), 4.50 (t, 2 H), 3.11 (t, 2 H).

Synthesis of DBP

S1 (0.85 mmol, 726 mg), S2 (1.00 mmol, 663 mg), S3 (0.15 mmol, 79 mg), tri (o-tolyl) phosphine (P(o-tol)$_3$, 0.78 mmol, 24 mg), tris (dibenzylideneacetone) dipalladium (DBa_3Pd_2, 0.019 mmol, 18 mg) were added to 50 mL toluene. The mixed solution was then reacted for 5 h at 50 °C under N_2 protection. After the reaction, the mixture was allowed to cool naturally. The reaction mixture was subsequently dropped into 500 mL of anhydrous methanol (MeOH). After filtration, a blue-green precipitate with metallic luster (DBP) was obtained. The degree of polymerization was analyzed by ^{1}H NMR. The molecular weight of the polymer was characterized by GPC.

Synthesis of APs

The heat sensitive linker 4,4′-Azobis(4-cyano-1-pentanol) (2.00 mmol, 504 mg), and 1,2,4,5-Cyclohexanetetracarboxylic acid dianhydride (2.11 mmol, 472 mg) were added to 5 mL anhydrous DMF. After 12 h, $mPEG_{5000}$-OH (2 mmol, 1000 mg) was introduced into the reaction system. Following 24 h of reaction time, the reaction mixture was added into 15 mL of deionized water under sonication, and subsequently dialyzed in a dialysis bag (MWCO: 8k Da) for 2 day. The resulting reaction mixture was freeze-dried under reduced pressure to obtained a light white polymer, designtated as AP_0.

AP_0 (1000 mg), 1-(3-dimethylaminopropyl)-3-ethylcarbodiimide hydrochloride (EDC, 4 mmol, 620 mg), N-Hydroxy succinimide (NHS, 4 mmol, 460 mg) and 3-({[(2-methyl-2-propanyl)oxy]carbonyl}amino)-*D*-alanine (Boc-*D*-aminoalanine) were added to 10 mL anhydrous DMF. The reaction system was divided into three groups, each receiving different amounts of Boc-*D*-aminoalanine:10 mmol (204 mg), 20 mmol (408 mg), and 30 mmol (612 mmg). After 12 h of reaction, the mixture was dialyzed in a dialysis bag (MWCO: 8k Da) for 2 days. The resulting solution was then freeze-dried under reduced pressure to obtained light white polymer, designtated as Boc-AP_1-AP_3.

Boc-AP_1-AP_3 (1000 mg) was dissolved in a mixed solution of 10 mL DMF/trifluoroacetic acid (TFA, *v/v*, 2/1), After 2 h of reaction, the mixture was dialyzed in a dialysis bag (MWCO: 8k Da) for 2 day. The resulting solution was then freeze-dried under reduced pressure to obtained light white polymer, designtated as AP_1-AP_3. The degree of polymerization was analyzed by ^{1}H NMR. The molecular weight of the polymer was characterized by GPC.

Preparation of nanoparticle

APs (AP_3 or AP_1, 5 mg) and DBP (1 mg) were dissolved in 1 mL DMF. With rapid stirring, 5 mL of water was added to the mixture to fabricate nanoparticles (NPs or DA_3-NPs). The resulting nanoparticles were purified by dialysis against water for 24 h. The size and zeta potential data of the nanoparticle were obtained through dynamic light scattering (DLS, Malvern Zetasizer NanoZS90). The morphology of the nanoparticles was observed through TEM testing.

Bacterial strains

The methicillin-resistant *Staphylococcus aureus* isolate strain (MRSA-1857) used in this study was isolated from the Affiliated Hospital, Academy of Military Medical Sciences (China). The MRSA cells were cultured and proliferated in a TSB medium at 37°C with a shaking speed of 180 rpm. After culturing, they were preserved by storing them on TSA plates at 4°C.

Colocalization between planktonic bacteria and nanoparticle

MRSA cells were incubated with FITC (1.0 μL, 1.0 mg/mL) for 3 h, after which they were centrifuged at 3500 rpm and washed 3 times. Following this, NPs/DA_3-NPs loaded Nile red (1.0 μL 1.0 mg/mL) were introduced into the MRSA suspension and incubated for 6 h at 37°C with a shaking speed of 180 rpm. The targeting effect of NPs/DA_3-NPs on MRSA was determined using flow cytometry and LSCM.

The MRSA suspension was diluted to a specific concentration of 5×10^5 CFU/mL in PBS. After that, the MRSA suspension (5×10^5 CFU/mL) was added to each well of a 96-well plate (100 μL per well) and then placed in a 37°C incubator. Following a 24 h incubation period, the TSB culture medium was replaced. After another 24 h incubation period, the TSB culture medium was removed to obtain a mature MRSA biofilm. The mature MRSA biofilms were treated with PBS, NPs, and DA_3-NPs for 6 h. At the end of the co-incubation of the material with the biofilm, the biofilm was washed three times with PBS. The concentration of NPs and DA_3-NPs was set at 32.5 μg/mL. Additionally, the groups of PBS+L, NPs+L, and DA_3-NPs+L were subjected to irradiated with an 808 nm laser at 0.33 W/cm^2 for 10 min, respectively. Subsequently, a crystal violet (CV) solution (1.0 mg/mL) was added to each well of a 96-well plate (200 μL per well). The plate was incubated for 30 min to allow staining, after which the CV solution was removed. Once completely

dry, 95 % ethanol was used for dissolution, and then 100 μL of ethanol was transferred to measure the optical density (OD) value at 595 nm.

The biofilms permeation of the nanoparticles

The MRSA biofilm was cultivated in a transwell chamber (pore size: 0.22 μm). Once the biofilm matured, NPs/DA_3-NPs solution (1.0 mL, 1.0 mg/mL, PBS buffer) was added above the transwell chamber. The concentration of NPs/DA_3-NPs in the receiver plate was measured using UV absorption at different times (3 h, 6 h, and 12 h).

Colocalization between bacteria within biofilm and the nanoparticles

The NPs/DA_3-NPs (1.0 mg/mL, prepared in PBS buffer) loaded with FITC were added to the confocal culture dish. After 6 h, the NPs/DA_3-NPs were removed, and then the DDAO and DAPI (1.0 μL, 1.0 mg/mL) were added to a confocal culture dish with mature MRSA biofilm, staining for 30 min. The treated biofilm was washed three times with PBS. Subsequently, the treated biofilm was observed using CLSM. Subsequently, the targeting effect of the NPs/DA_3-NPs on bacteria within the biofilm was determined by flow cytometry analysis. The mature MRSA biofilm was cultivated in 48 wells. The NPs/DA_3-NPs (loaded with Nile, 1.0 mL, 1.0 mg/mL, prepared in PBS buffer) and FITC (1.0 μL, 1.0 mg/mL) were added to the 48 wells. After 6 h, the 48 wells containing mature MRSA biofilm were washed thrice with PBS. Finally, MRSA suspensions were collected in 48-well plates by adding PBS (1 mL) and subjected to ultrasonic treatment for 1 h.

Establishment of animal models

In vivo biofilm-infection wound model: Balb/c female mice were first anesthetized. Subsequently, a wound with a size of 1.0 cm^2 was created on the back of each mouse and secured with sterile patches. On day 1, post-wounding, the shape of the wound was fixed and no longer changed. Then, a bacterial suspension of MRSA (200 μL, 1×10^9 CFU/mL) was injected onto the wound's surface. On day 2, the TSB culture medium (200 μL) was replenished on the wound's surface. On day 3, a white mucous membrane (MRSA biofilm) was observed on the wound's surface, confirming the successful establishment of the *in vivo* biofilm-infection wound model.

In vivo catheter biofilm model: the catheter (10 mm) was co-cultured with MRSA suspension (5×10^5 CFU/mL) in 48-well plate to allow the formation of the mature biofilm. Once the MRSA biofilm had matured on the catheter, the catheter containing the MRSA biofilm was implanted into the back of Balb/c female mice to establish the catheter biofilm model.

Mice treatment

All treatment groups were established, including PBS+L, NPs, NPs+L, DA_3-NPs, and DA_3-NPs+L groups. For each group, three mice were used as parallel controls. The laser power and irradiation time were standardized at 0.33 W/cm^2 and 10 min for all experimental conditions.

In vivo biofilm-infection wound model: the time of successful animal model establishment was marked as day 0. On days 1–3, DA_3-NPs and NPs were intravenously injected 3 times (3 mg/kg per time). On day 4 and 5, laser irradiation was applied to mice in the PBS+L, NPs+L and DA_3-NPs+L groups.On days 6–11, continuous observations and photography were conducted to monitor changes in the infected wound site and the body weight of mice. On day 11, mice were euthanized under anesthesia at the end of the treatment period. Tissue samples from the infection site were surgically excised from the mice and fixed in a 4 % fixative solution. Subsequently, the infected tissues were stained with Gram stain and H&E stain, followed by then examination using a digital microscope.

In vivo catheter biofilm model: the time of successful animal model establishment was designated as day 0. On days 1 and 2, DA_3-NPs and NPs were locally administered twice (3 mg/kg per time). On Day 3, laser irradiation was applied to mice in the PBS+L, NPs+L, and DA_3-NPs+L groups. On days 4–7, continuous observations and photography were conducted to monitor changes in the body weight of mice. On Day 7, the implanted catheter was removed and stained to observe the biofilm and surrounding tissue. Subsequently, the remaining steps were the same as described above.

Statistical analysis

The data was expressed as mean ± standard deviation (s.d.). The student's T-test was performed to determine the statistical difference between groups. $n \geq 3$, ns $p > 0.05$, * $p < 0.05$, ** $p < 0.01$, *** $p < 0.001$ and **** $p < 0.0001$.

Results and discussions

Preparation and characterization of DA_3-NPs

A phototherapeutic polymer (namely DBP) consisting of 3 parts was designed (Scheme S1). The key component was 4,4′-(5,5-difluoro-2,8-diiodo-3,7-bis(4-methoxyphenyl)-5*H*-4λ^4,5λ^4-dipyrrolo [1,2-*c*:2′,1′-*f*] [1–3,5] triazaborinine-1,9-diyl) bis(*N*,*N*-diethylaniline) (defined as S1) that possessed strong fluorescence and PDT/PTT effect. The second part was 5,6-difluoro-4,7-bis (5-(trimethylstannyl) thiophen-2-yl) benzo [c] [1,2,5] thiadiazole (defined as S2). The thiophene structure in S2 acted as an electron donor and an π bridge for electron transfer either, which narrowed the bandgap *via* strong electron absorption ability and resulted in redshift of wavelength absorption and increased ROS yield of photodynamic [32]. Additionally, a GSH-sensitive monomer (S3) was introduced into DBP. This endowed DBP with biodegradability within the biofilm microenvironment (Fig. 1a). DBP structure was confirmed by ^{1}H NMR and GPC spectrometry (Scheme S1 & Figs. S1–5).

As shown in Fig. 1b, the UV absorption of DBP appeared at 599 nm, 601 nm, and 889 nm, while its fluorescence emission appeared at 1121 nm, indicating the near-infrared II (NIR-II) fluorescence properties of DBP. Under laser irradiation (808 nm, 0.33 W/cm^2), DBP possessed a discernible photothermal effect, and the photothermal effect exhibited a concentration-dependent pattern (Fig. 1c). To assess the photothermal stability of DBP, high concentrations of DBP were exposed intermittently to laser irradiation. DBP exhibited good thermal stability within 5 cycles of irradiations (Fig. S6). Additionally, DBP played an important role in PDT. DBP could be excited to a singlet state (S_1) under laser irradiation. After intersystem crossing to generate a triplet excited state (T_1), the energy was transferred to the surrounding O_2 to form ROS [33]. Thus, electron paramagnetic resonance (EPR) was used to detect free radicals generated by DBP, in which DBP generated a classic peak shape of singlet oxygen ($^1O_2$) under laser irradiation (Fig. 1d) [34]. Thereafter, a quantitative analysis of the generation rate of $^1O_2$ by DBP was conducted using the classical probe 1,3-diphenylisobenzofuran (DPBF) [35]. After coincubation with DBP under laser irradiation (denoted as DBP+L), DPBF exhibited a rapid decrease in UV absorption (425 nm) (Fig. S7), indicating the generation of $^1O_2$ by DBP+L. After calculation, the DPBF decomposition rate in the DBP solution exhibited a linear relationship with laser irradiation time (Fig. 1e). The DPBF decomposition rate constant in samples of DBP+L and DBP were 1.02×10^{-3} s^{-1} and 5.98×10^{-5} s^{-1}. This indicated that DBP+L has a good ROS yield, which could be used as an adjuvant for PDT. These results implied that DBP possessed promising potential as a NIR-II PAs.

To enable DBP use for biofilm elimination *in vivo*, an amphiphilic thermosensitive azo polymer (denoted as APs) was synthesized and applied to encapsulate DBP. The successful synthesis of a series of APs was demonstrated by ^{1}H NMR and GPC spectra (Scheme S2 & Fig. S8-13). In particlular, the *D*-aminoalanine group was used to endow APs with bacterial targeting ability and adjustable electrical properties [36].

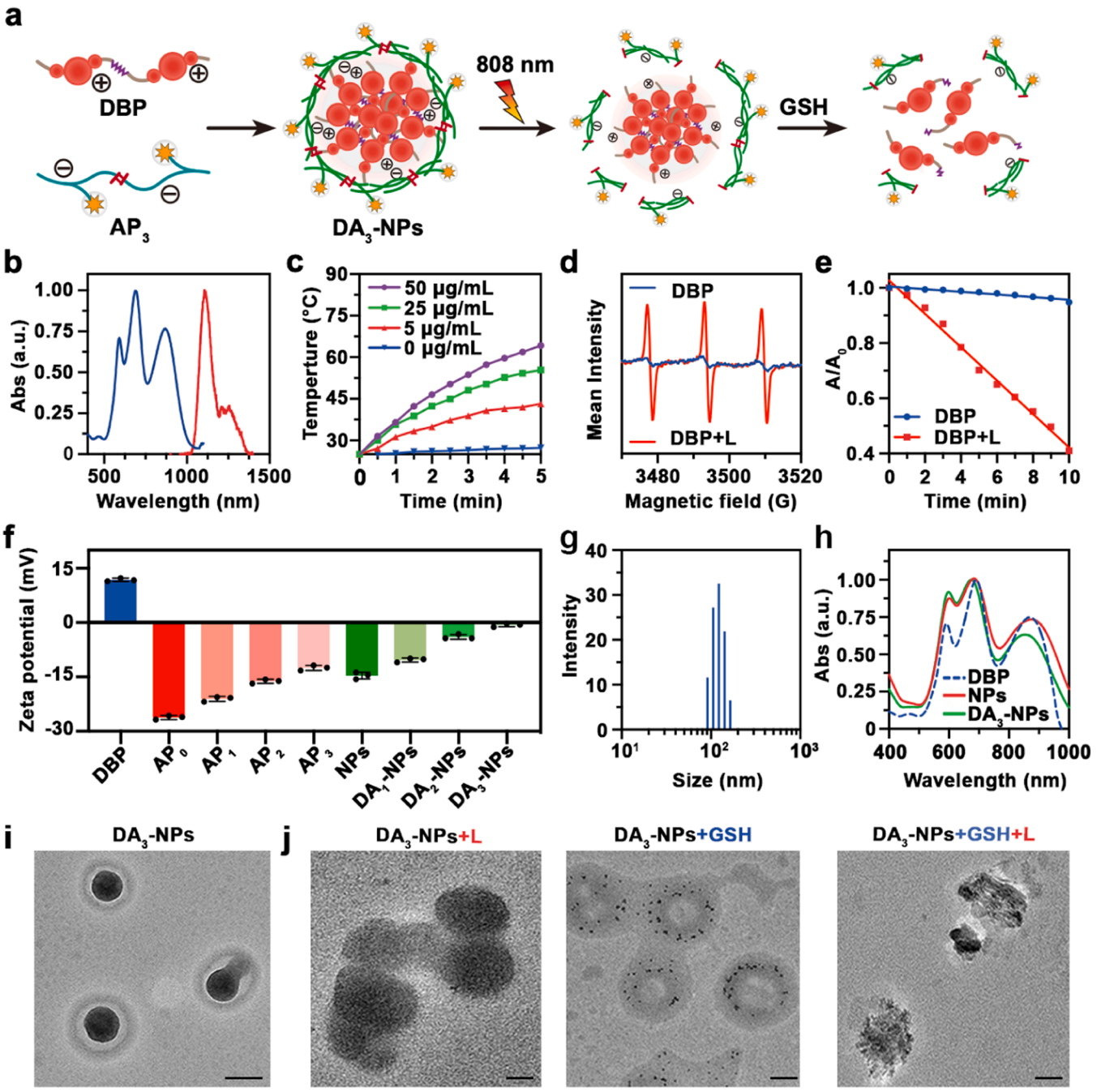

Fig. 1. Characterization of DBP, AP_3 and DA_3-NPs. (a) Schematic illustration of the assembly and degradation behaviors of DA_3-NPs. (b) The excitation-emission spectrum of DBP. (c) The corresponding heating curve of DBP under 808 nm laser irradiation (0.33 W/cm^2, 5 min). (d) EPR spectrum of DBP and DBP+L (808 nm, 0.33 W/cm^2, 10 min). (e) Normalized time-dependent UV–vis absorbance at 415 nm of DPBF in the presence of DBP and DBP+L (808 nm, 0.33 W/cm^2, 10 min). (f) Zeta potential of DBP, APs and particles in PBS. (g) Particle size distribution of DA_3-NPs. (h) UV–vis absorption spectra of DBP, NPs and DA_3-NPs. (i) TEM image of DA_3-NPs. Scale bar: 100 nm. (j) TEM images of DA_3-NPs+GSH, DA_3-NPs+L and DA_3-NPs+GSH+L (GSH concentration = 10 mM, irradiation conditions: 808 nm, 0.33 W/cm^2, 10 min). Scale bar = 50 nm.

By regulating the reaction formulas, the grafting ratios of *D*-aminoalanine in AP_0, AP_1, AP_2 and AP_3 were 0.0, 23.1, 38.5 and 76.9 %, respectively (Table S1). Their zeta potential could be changed from –25.6 mV (AP_0) to –12.8 mV (AP_3) (Fig. 1f). Subsequently, APs were co-assembled with DBP to form stable nanoparticles. Because DBP possessed a positive charge of 11.3 mV, while AP_3 possessed an opposite charge of −12.3 mV, the obtained DA_3-NPs, therefore, exhibited a neutral charge of −0.61 mV, which is critical for their penetration of biofilm. The size of DA_3-NPs was ~149 nm with a polydispersity index (PDI) of 0.111 (Fig. 1g). Similarly, when AP_0 without *D*-aminoalanine groups was used as an alternative of AP_3 to co-assemble DBP (denoted as NPs), the obtained NPs was ~153 nm with an obvious negative charge of −11 mV. The stability assay demonstrated that both DA_3-NPs and NPs were stable in PBS and FBS and did not show obvious changes within 7 days (Fig. S14). In the UV-absorption spectra (Fig. 1h & Fig. S15), a slight blue-shift absorption of DA_3-NPs could be observed compared with that of NPs, which was potentially attributed to the introduction of *D*-aminoalanine groups leading to H-aggregation of DBP [37]. This further indicated that the assembly of DA_3-NPs might be driven by the charge interactions between DBP and AP_3. Interestingly, an obvious

core-shell morphology of DA_3-NPs could be observed in the TEM image, in which the core was dense while the shell was loose (Fig. 1i). This was in agreement with the UV–vis results that the core might be formed by the aggregated DBP, and the shell might be formed by the AP_3.

Accordingly, the specific core-shell structure of DA_3-NPs could be further illustrated because of the GSH- and thermal-responses of DBP and AP_3, respectively. Firstly, GPC was employed to monitor the molecular weight changes of DBP and AP_3. As shown in Fig. S16, the elution time of the DBP (treated wiht 10 mM GSH) and the AP_3 (treated by 50 °C heating) gradually increased [38], indicating the decrease in their molecular weights. DBP was degraded because its −S−S− structure was broken by GSH, and over 80 % of GSH could be consumed by DBP (10 mg/mL) within 12 h (Fig. S17). This capacity was in favor of enhancing the photodynamic effect of DBP. The azo structure in AP_3 was thermal-responsive. Its thermal degradation could generate substantial carbon free radicals (Fig. S18). Thereby, the generation of carbon-free radicals could be detected by using the testing reagent 2,2'-azino-bis (3-ethylbenzothiazoline-6-sulfonic acid) (ABTS) [39]. When AP_3 was heated at 50 °C, carbon-free radicals were rapidly generated, and the produced $ABTS^{+}\bullet$ displayed an increased UV–vis absorption in a short

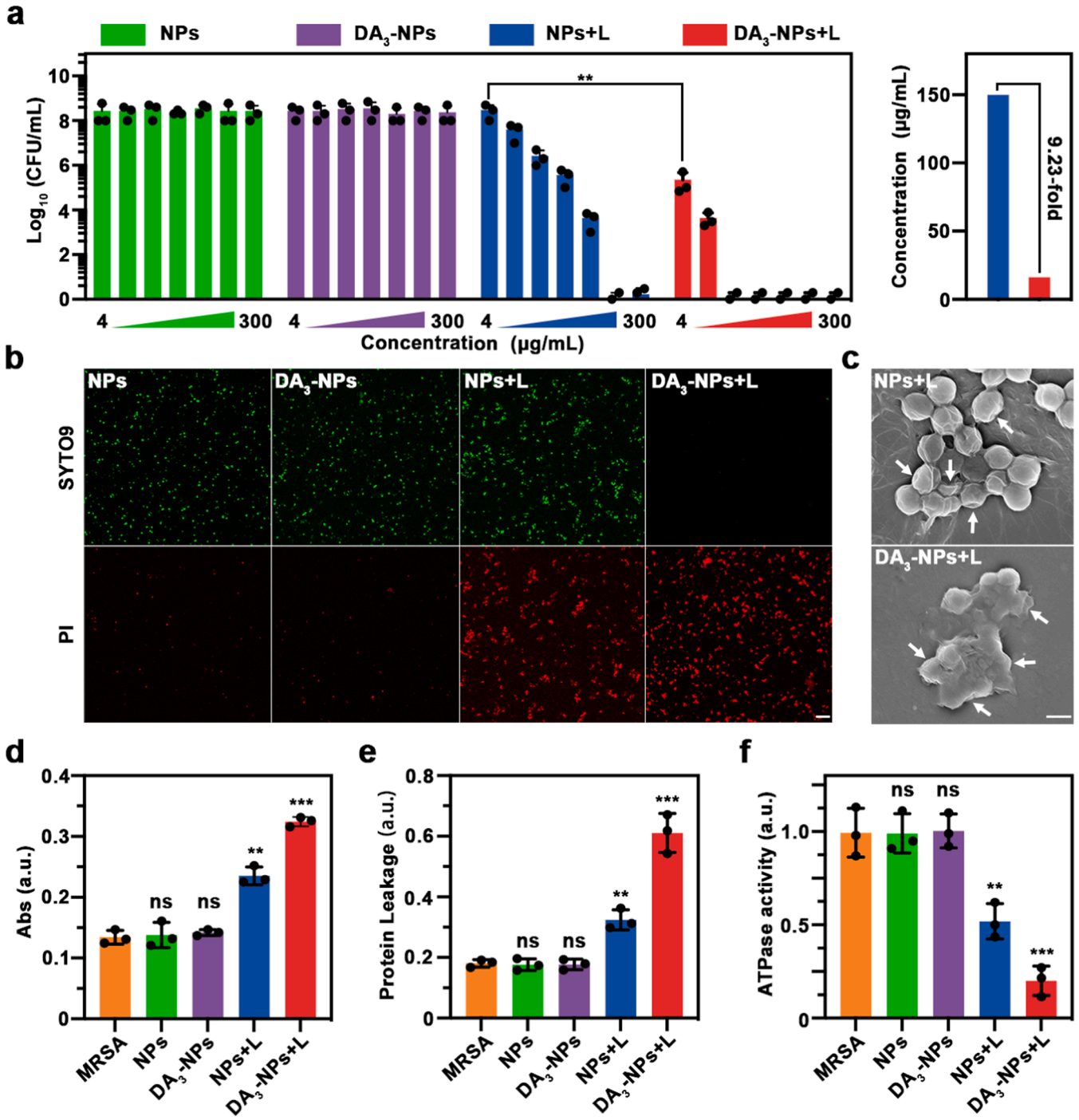

Fig. 2. Antibacterial activity of DA_3-NPs and NPs against planktonic MRSA. (a) MBC of different treatment groups. (b) Confocal images of SYTO9/PI-labeled MRSA after incubation with the treatments for 8 h. Scale bar = 10 μm. (c) SEM images of MRSA treated with different groups for 8 h, the white arrows represent sites of bacterial damage. Scale bar = 500 nm. (d) Membrane permeability, (e) protein leakage, and (f) ATPase activity of MRSA treated with different groups. Data are expressed as the mean ± SD, Student's t-test, n = 3, ns $p>0.05$, * $p<0.05$, ** $p<0.01$, and *** $p<0.001$.

time (Fig. S19). Additionally, the azo structure acting as a pusher electron group exhibited a *p-π* conjugation effect. Upon degradation, the electron-pushing effect disappeared, but the strong electron-withdrawing cyanide group would still exist, leading to a notable chemical shift that could be captured on the ^{1}H NMR spectrum. Therefore, this structural change of AP_3 was illustrated by using an AP_3 derivative. As shown in Fig. S20, the proton H_1 of the AP_3 derivative underwent a significant chemical shift when increasing temperature, while alkanes generated by carbon-free radicals could be gradually detected, further confirming the thermal response of AP_3. Predictably, these robust properties of DBP and AP_3 would endow DA_3-NPs with the capacity of GSH- and thermal-responsive. Accordingly, the morphological changes of DA_3-NPs upon GSH or thermal stimulation were observed. TEM images (Fig. 1j) clearly showed that the external shell structure disappeared completely after heating, while upon the intensive treatment of high-does GSH (10 mM, 12 h), the internal dense core structure disintegrated into fragments, but the outer shell structure remained. After the treatment of laser irradiation and GSH incubation, DA_3-NPs disassembled and showed a disintegrating spherical morphology, confirming the specific core-shell structure of DA_3-NPs, and their feasible stimuli-responsive properties.

In vitro antibacterial properties and mechanism

Subsequently, the antibacterial efficacy of DA_3-NPs was comprehensively assessed, and NPs were used as the control group. As shown in Fig. 2a, DA_3-NPs and NPs alone could not kill planktonic MRSA (MRSA-1857) regardless of their concentration. Under laser irradiation (808 nm, 0.33 W/cm^2, 10 min), NPs (denoted as NPs+L) performed phototherapeutic capacity and resulted in a dose-dependent bactericidal effect. Its minimum bactericidal concentration (MBC) was determined to be 150 μg/mL. Notably, DA_3-NPs with laser irradiation (denoted as DA_3-

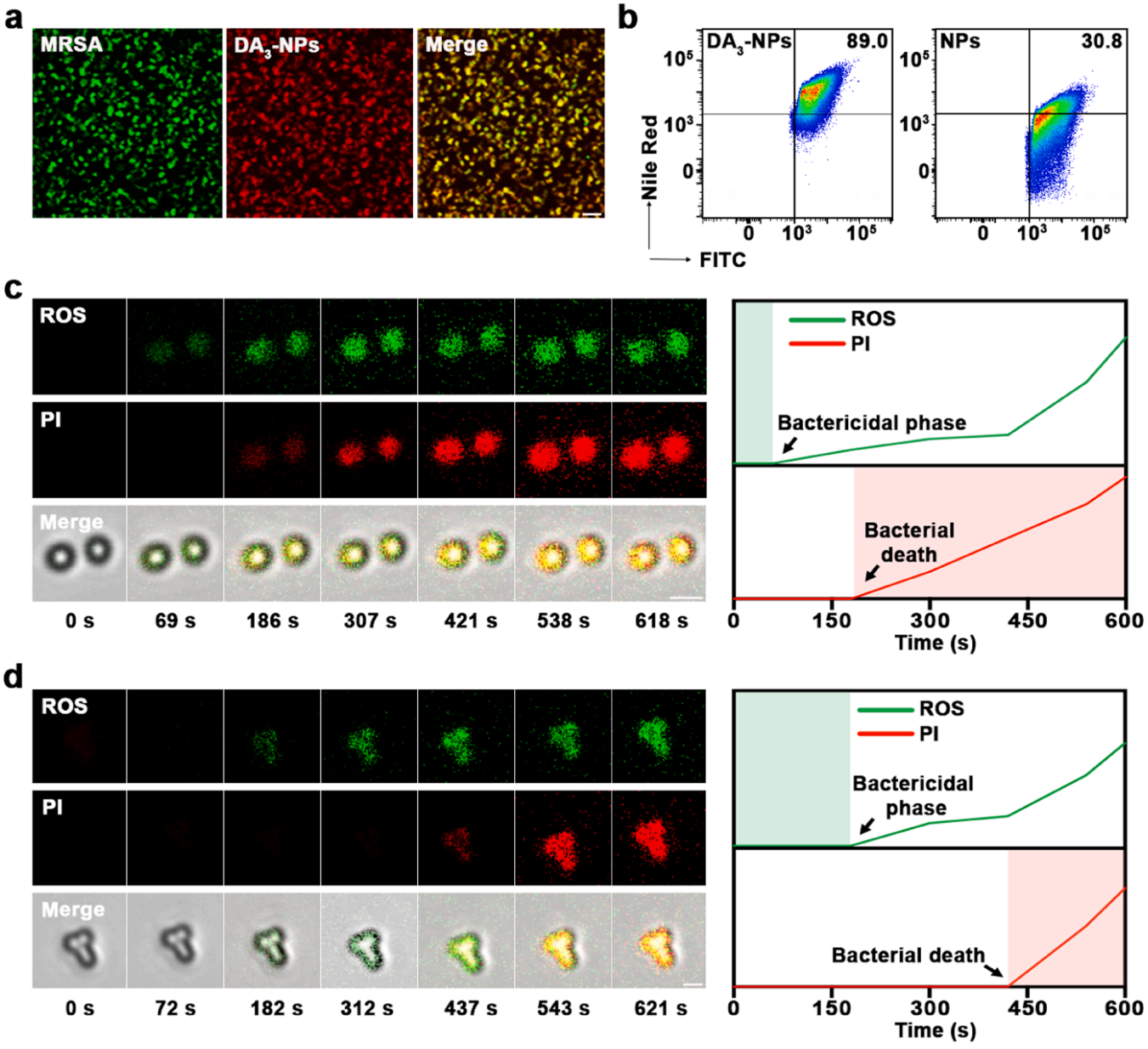

Fig. 3. Antibacterial mechanism of DA_3-NPs against planktonic MRSA. (a) Confocal images of FITC-labeled MRSA after incubation with Nile red-labeled DA_3-NPs. Scale bar = 5 μm. (b) Flow cytometry assay of the FITC-labeled MRSA after incubation with Nile red-labeled DA_3-NPs and NPs. Confocal images of the stained MRSA after incubation with (c) DA_3-NPs and (d) NPs under 808 nm laser irradiation (0.33 W/cm^2, 10 min). Scale bar = 500 nm. The curves on the right side were the time-dependent fluorescence distribution profiled in the groups of DA_3-NPs+L and NPs. The concentration of DA_3-NPs and NPs was 2 × MIC.

NPs+L) displayed remarkable bactericidal performance and completely killed MRSA at 16.25 μg/mL (Fig. S21), which was 9.23 times lower than NPs+L. Bacterial live/dead detection (Fig. 2b & Fig. S22) confirmed that MRSA was active and accompanied by strong green fluorescence after the treatment of PBS+L, NPs, and DA_3-NPs; while NPs+L showed enhanced bactericidal ability, resulting in increased red fluorescence of the treated MRSA. In contrast, the MRSA treated by DA_3-NPs+L was completely killed and showed strong red fluorescence. SEM images showed that the cell walls of the MRSA exhibited remarkable collapse and rupture (Fig. 2c). The investigation of bactericidal mechanism revealed that the treatments of DA_3-NPs+L (20 μg/mL) could significantly increase the bacterial membrane permeability, cause protein leakage and decrease ATPase activity of the treated MRSA (Fig. 2d & f). Comparatively, NPs+L (20 μg/mL) exhibited a similar but significantly lower antibacterial effect than DA_3-NPs+L. This implied that the targeting ability might enable DA_3-NPs to anchor on the bacterial surface, and subsequently generated ROS, carbon radicals and heat damage under laser irradiation to kill MRSA effectively and precisely.

In-situ antibacterial mechanism

Accordingly, the antibacterial mechanisms of DA_3-NPs and NPs were comprehensively studied by using a classic ROS probe. The LSCM results demonstrated DA_3-NPs in red fluorescence (Nile red was loaded in DA_3-NPs) overlapped well with the MRSA in green fluorescence (MRSA was stained with FITC) and exhibited a high co-localization (Fig. 3a & Fig. S23). Flow cytometry assay revealed that the targeting efficiency of DA_3-NPs for MRSA was as high as 89.0 %, which was approximately 2.88 times higher than that of NPs (30.8 %, Fig. 3b). Subsequently, the real-time antibacterial performance of DA_3-NPs was monitored. The classic ROS probe 2′,7′-dichlorodihydrofluorescein diacetate (DCFH-DA), and propidium iodide (PI) were used to treat planktonic MRSA [40,41]. Then, the MRSA was co-incubated with the particles and irradiated by laser for 10 min. After that, the treated MRSA was monitored using LSCM time-lapse photography. As Fig. 3c shown, the planktonic MRSA with green fluorescence could be detected at 69 s upon DA_3-NPs+L treatment, and the fluorescence intensity gradually increased with time, suggesting ROS accumulation in the MRSA. At 186 s, the MRSA was killed accompanied by red fluorescence detection at this time. For NPs+L groups (Fig. 3d), ROS accumulation in the MRSA could be observed at 182 s, and the MRSA died at 437 s. The fluorescence intensity profiles (Fig. 3c & d) clearly illustrated that bacterial killing in DA_3-NPs+L treatment were much faster than those in NPs+L treatment. Furthermore, the accumulation of ROS on bacterial cells in the DA_3-NPs+L group was much higher than that in the NPs+L group within ~180 seconds (Fig. S24). This fully demonstrated that the targeting property of DA_3-NPs+L accelerated the accumulation of ROS as well as the generation of carbon radicals and heat damage on the surface of the bacterial surface, resulting in the enhancement of the bactericidal efficacy.

In vitro anti-biofilm properties and mechanism

The antibacterial and targeting performances toward planktonic MRSA greatly inspired us to utilize DA_3-NPs for the study of anti-biofilms. The effective biofilm penetration and internal MRSA targeting were crucial for eradicating biofilms by *in-situ* phototherapy [42,43]. Therefore, the biofilm penetration of DA_3-NPs was first assessed. As shown in Fig. 4a, a transwell model was used to quantify the biofilm penetration efficiency of DA_3-NPs and NPs. The results indicated that only a few NPs could penetrate the biofilm regardless of increasing concentration and treatment time, whereas DA_3-NPs could effectively penetrate the biofilm within 3 h, and the penetration effect of DA_3-NPs was positively correlated with treatment time and the concentration of DA_3-NPs (Fig. 4b). This implied that DA_3-NPs exhibited a strong capacity for biofilm penetration, which might be attributed to their properties of small particle size, neutral charge and bacterial targeting. Firstly, DA_3-NPs possessed small particle sizes (~ 149 nm, Fig. 1g), facilitating their passage through the polysaccharides and lipids of EPS [44,45]. Secondly, the neutral or positive charge of nanoparticles enhances biofilm penetration because the EPS of biofilms is negatively charged [46,47]. The grafting ratios of *D*-aminoalanine in APs were regulated to obtain the electroneutral DA_3-NPs (–0.61 mV). Compared to NPs (–11 mV), DA_3-NPs could penetrate biofilms more easily without electric charge repulsion. Thirdly, the bacterial targeting capacity of DA_3-NPs promoted the biofilm penetration [30]. Bacterial targeting within the biofilm would provide a strong impetus to accelerate DA_3-NPs into the interior of the biofilm. Accordingly, the targeting effect of DA_3-NPs toward MRSA within biofilm was assessed by LSCM [48]. EPS of the biofilm was stained by dimethylaminoazobenzene oxide (DDAO) with a red fluorescence, and the MRSA within the biofilm was stained by DAPI with a blue fluorescence [49]. After treatment by DA_3-NPs@FITC (FITC was loaded into DA_3-NPs) with green fluorescence, a 3-dimensional (3D) confocal image of a 60 μm-thick biofilm could be reshaped. As shown in Fig. 4c, DA_3-NPs@FITC effectively penetrated the EPS and exhibited perfect fluorescence overlap with the MRSA in the biofilm. In contrast, when the biofilm was treated with NPs@FITC, the weak green fluorescence of NPs@FITC was mainly confined to the surface of the biofilm, while minimal and negligible red fluorescence was detected within the biofilm. In particlular, the colocalization between the nanoparticles and MRSA within the biofilm was comprehensively assessed (Fig. 4d & e). The stereo space vision of 3D confocal images showed that the green fluorescence signals of DA_3-NPs@FITC matched well with the blue fluorescence of MRSA in the entire dense biofilm (Fig. 4f). The Pearson's correlation coefficient (PCC) reached up to 0.93 within biofilm (Fig. 4g). In comparison, the NPs@FITC was stuck on the surface of the biofilm, and was independent with the location of the MRSA (Fig. 4e & g). The flow cytometry assay results further revealed that the targeting efficiency of DA_3-NPs towards the internal MRSA was as high as 70.6 %, while that of NPs was only 8.3 %, which was 8.51 times lower than that of DA_3-NPs (Fig. 4h). These results strongly suggested that the proposed DA_3-NPs has an excellent targeting activity toward MRSA within the biofilm.

Bacterial targeting was critical for the *in-situ* phototherapy of DA_3-NPs, which would allow the accumulation of ROS, carbon radicals and heat damage focusing on the internal bacteria [50]. Considering that the commonly used methods for thermal monitoring, such as infrared thermal imaging and thermal sensors, are difficult to observe at the micron level, the distribution of ROS within the biofilm, therefore, was studied by using a fluorescent probe. After 6 h of co-incubation, the particles were washed away, and the treated biofilms were irradiated by an 808 nm laser (0.33 W/cm^2) for 10 min. Subsequently, the generated ROS in the biofilm was observed by LSCM. In the DA_3-NPs+L group, the generated ROS with green fluorescence distributed uniformly in the whole biofilm and overlapped well with the bacterial residence in blue fluorescence (Fig. 5a). Quantitative analysis showed that the accumulation of the ROS was positively correlated with the bacterial count, suggesting the ROS could be fully utilized to kill bacteria and thus remarkably reinforced the anti-biofilm efficacy of DA_3-NPs+L. Conversely, the ROS generated by NPs+L was mainly trapped on the surface of the biofilm and showed no overlap with the internal bacteria (Fig. 5b). To further illustrate the efficacy of *in-situ* phototherapy, a comparative experiment on the elimination effects of NPs+L and DA_3-NPs+L against mature MRSA biofilms was conducted. As shown in Fig. 5c, the biofilm-elimination performance of DA_3-NPs+L was positively correlated with the dosage and the laser irradiation time. When the dosage of DA_3-NPs was 2 × MIC (32.5 μg/mL), 9 min laser irradiation could eliminate 97.1 % of the mature MRSA biofilm; while its dosage was 20 × MIC (325 μg/mL), the laser irradiation time could be shortened by 5 min to reach similar biofilm-elimination efficiency (97.9 %). However, NPs+L failed to eliminate the MRSA biofilm. Even though its dosage was up to 20 × MIC (3000 μg/mL) and the laser

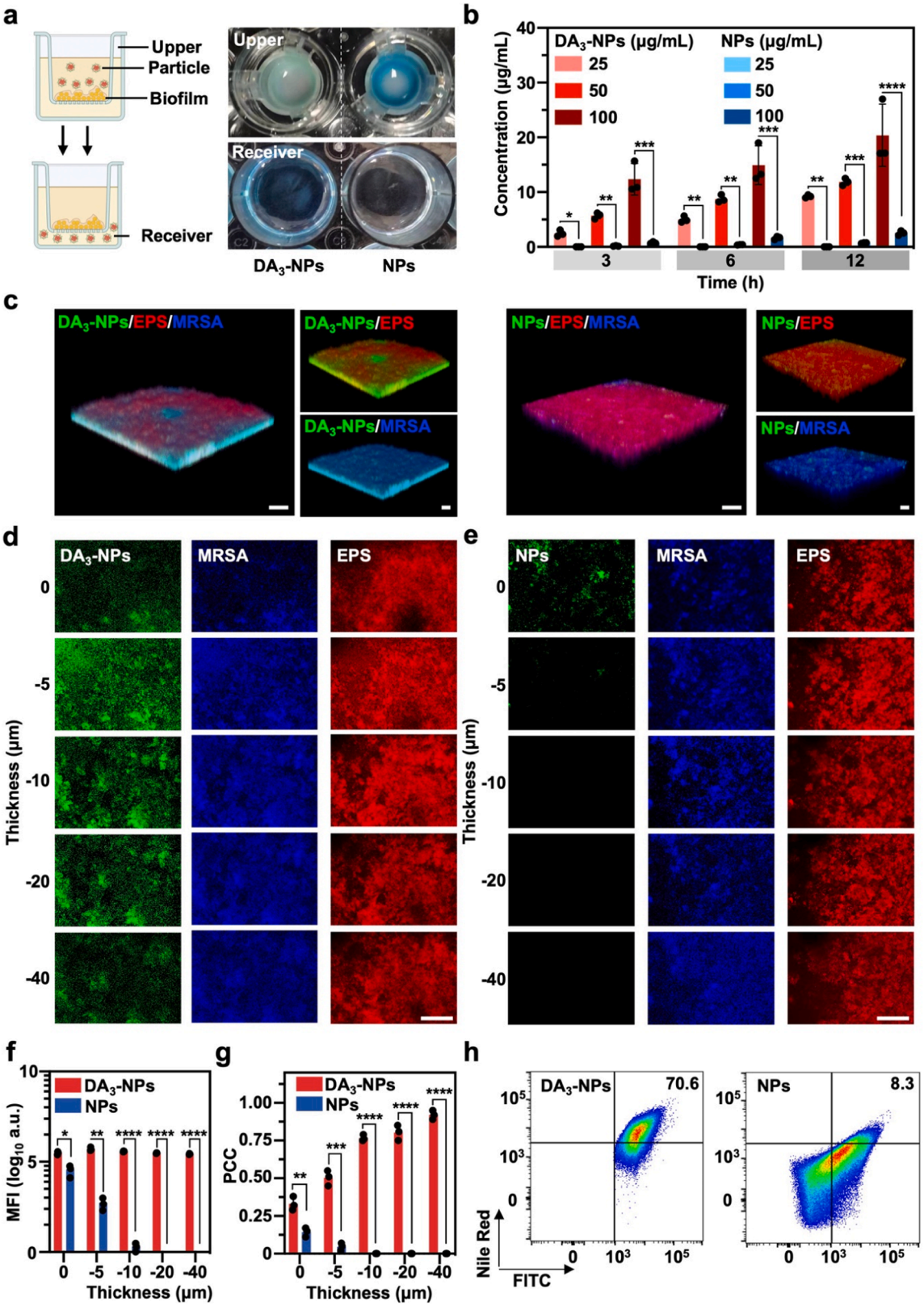

Fig. 4. *In-situ* targeting mechanism of DA_3-NPs towards MRSA within the biofilm. (a) Permeation effects of DA_3-NPs and NPs in biofilm. Scale bar = 50 μm. (b) Concentration statistics of DA_3-NPs and NPs in transwell receiver chambers. (c) 3D confocal images of the strained biofilm after incubation with FITC-labeled particles (red, blue and green fluorescences represented EPS, MRSA, and the particle, respectively). Scale bar = 50 μm. Confocal images of biofilm treated with (d) DA_3-NPs and (e) NPs. Scale bar = 50 μm. (f) Relative green fluorescence intensity of DA_3-NPs and NPs within the biofilm. (g) PCC value between the particles and the internal MRSA. (h) Flow cytometry assay of the FITC-labeled MRSA with the biofilm after incubation with the Nile red-labeled particles. Data are expressed as the mean ± SD, Student's t-test, n = 3, * $p<0.05$, ** $p<0.01$, *** $p<0.001$, and **** $p<0.0001$.

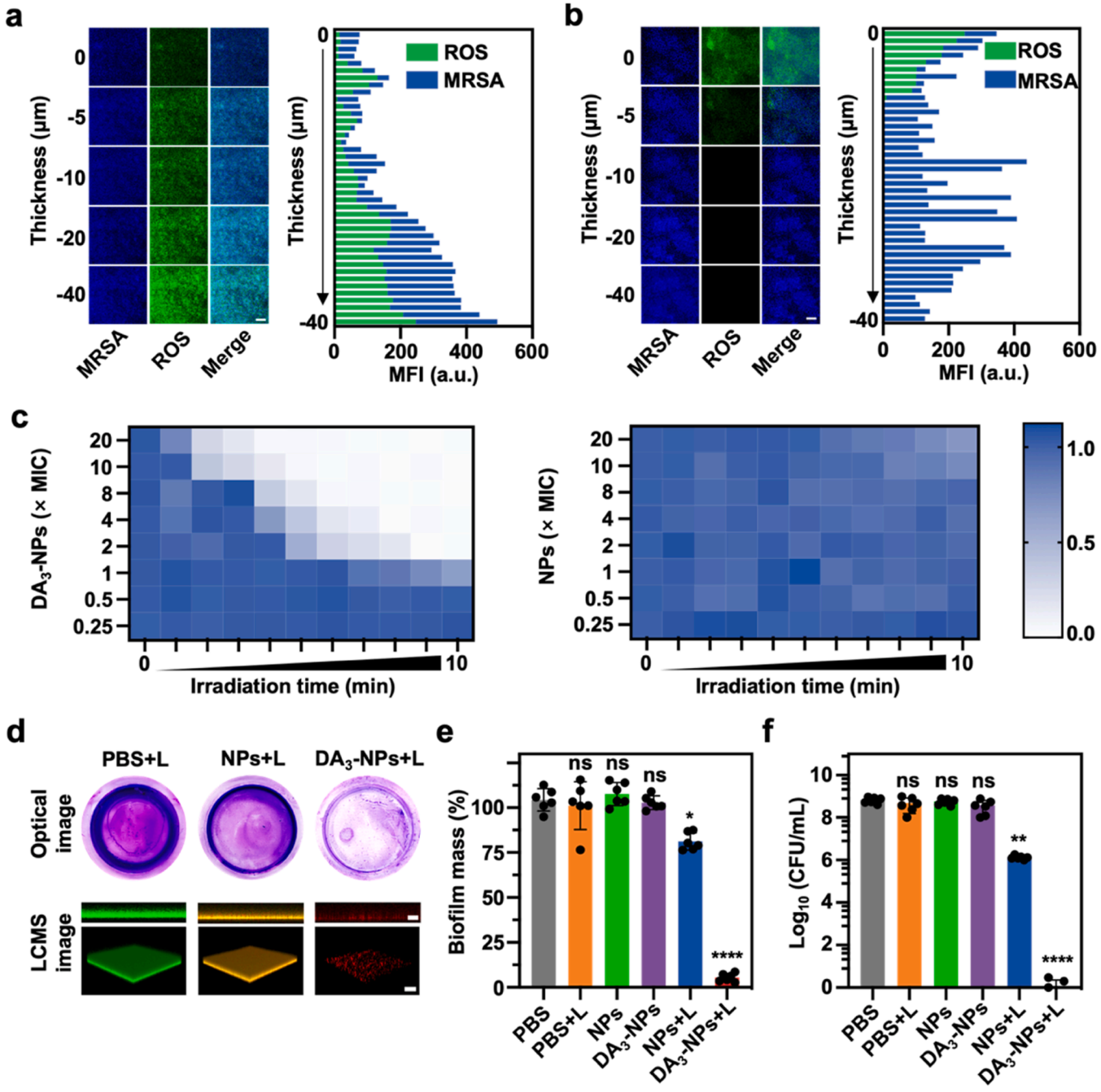

Fig. 5. *In vitro* biofilm elimination of DA_3-NPs and NPs. Confocal images of MRSA and ROS generated by (a) DA_3-NPs+L and (b) NPs+L. Scale bar = 50 μm. Blue fluorescence represented MRSA, and green fluorescence represented ROS. Laser irradiation conditions: 808 nm, 0.33 W/cm^2, 10 min. (c) The anti-biofilm activity of DA_3-NPs and NPs. (d) Optical and confocal images, (e) biofilm mass, and (f) bacterial counts of the biofilm treated by different groups. The concentration of DA_3-NPs and NPs was 2 × MIC. Scale bar = 50 μm. Data are expressed as the mean ± SD, Student's t-test, n = 6, ns $p>0.05$, * $p<0.05$, ** $p<0.01$, and **** $p<0.0001$.

irradiation time was extended for 10 min, its biofilm-elimination efficiency was ~50 %. Comparatively, when the treatment condition was restricted to 2 × MIC dosage and 9 min of laser irradiation, the biofilm-elimination efficiency of DA_3-NPs was at least 61 times higher than that of NPs, strongly suggesting the effectiveness of the *in-situ* phototherapy strategy in eliminating internal bacteria and eradicating biofilms.

Then, the eradication efficacy of mature biofilms by DA_3-NPs+L was studied. In crystal violet (CV) stain assay (Fig. 5d), dense biofilms in dark purple were observed in the group of PBS+L, while the biofilms in the group of NPs+L were partially removed and showed a faded purple color. Comparatively, DA_3-NPs+L effectively eliminated the mature biofilms, in which the residual biofilms displayed a weak purple color. Thereafter, the stained dead/live MRSA in biofilms was visualized by LSCM. The biofilms treated with PBS+L showed strong green fluorescence, indicating the internal bacteria still survived. The biofilms in the NPs+L group displayed bright yellow fluorescence, signifying substantial live bacteria within the biofilm. Differently, most of the bacteria within the biofilm were killed in the DA_3-NPs+L group and exhibited sparse red fluorescence. Statistical analysis of biofilm mass and bacteria count (Fig. 5e & f) further demonstrated the biofilm was exceedingly eradicated by DA_3-NPs+L, which significantly outperformed NPs+L.

In vivo biofilm-infection wound model

Two *in vivo* biofilm models (biofilm-infection wound model and catheter biofilm infection model) were used to assess the therapeutic effects of DA_3-NPs [51–53]. Based on clinical guidance for treating biofilm infections, two distinct *in vivo* biofilm infection models were established, employing varied administration methods to further validate the *in vivo* anti-biofilm activity of DA_3-NPs and NPs [47,54]. For the therapy of biofilm-infection wound, the model was first established by inoculating culture medium-grown MRSA (10^9 CFU/mL, 150 μL) in the wound of the mice. After 1 day, a distinct white mucous membrane would cover the wound, suggesting the successful modeling of the *in vivo* MRSA biofilm [55]. The infected mice were divided randomly into five groups (PBS+L, NPs, NPs+L, DA_3-NPS, DA_3-NPs+L), and the time was marked as day 0. Intravenous drug-administration (3 mg/kg per time) was conducted thrice on days 1–3, and then laser irradiation (808 nm, 0.33 W/cm^2, 10 min per time) was conducted twice on days 4 and 5 (Fig. 6a). During the treatment process, thermal imaging was collected to investigated temperature changes at biofilm infection site under laser irradiation (Fig. 6b). In the DA_3-NPs+L group, the temperature at the wound infection site rose to ~47°C upon laser irradiation, which was ~1.8 and ~8.6 times higher than those in the groups of NPs+L and PBS+L, respectively (Fig. 6c). This indicated that DA_3-NPs could effectively target and accumulate in the biofilm infection site. After the treatment of DA_3-NPs+L, the mice exhibited the fastest recovery (Fig. 6d). Their wound healing rate was much faster than those in the other treatment groups. The wounds were completely healed on day 11 without apparent bacteria and biofilm remained (Fig. 6e & f), suggesting the biofilm had been eliminated by DA_3-NPs+L. In contrast, there was no obvious difference in wound healing in the groups of PBS+L, NPs and DA_3-NPs. On day 11, the wound had not fully healed, and clear wound infections could be observed (Fig. 6f). The same phenomenon was observed in the mice treated with NPs+L. Although the NPs+L slightly reduced bacteria count, its anti-biofilm performance *in vivo* was limited (Fig. 6g). The weight change further supports the above results (Fig. S25).

Furthermore, Gram staining of the wound infection tissue was performed to further confirm the residual biofilm in the wound site (Fig. 6h). The results showed that a large number of tissue with dark purple color (blue arrows) appeared in the groups of PBS+L, NPs, DA_3-NPs, and NPs+L. The presence of purple tissue indicates an infection caused by Gram-positive bacteria (MRSA) [56]. Comparatively, only limited tiny purple tissue appeared in the DA_3-NPs+L group. This meant that the DA_3-NPs+L group could eliminate most MRSA biofilm *in vivo*. Finally, hematoxylin and eosin (H&E) staining was used to observe the inflammatory cells and healing at the infection site [57]. The results indicated that many inflammatory cells (green arrows) were observed in the groups of PBS+L, NPs, and DA_3-NPs. In the NPs+L group, the inflammatory cells did not completely disappear, but a healed skin tissue layer was observable. In the DA_3-NPs+L group, the tissue had returned to normal with negligible inflammatory cell infiltrations, suggesting DA_3-NPs+L were highly effective in eradicating the biofilm *in vivo*.

In vivo catheter biofilm model

Additionally, an *in vivo* catheter biofilm infection model was used to further assess the therapeutic effects of DA_3-NPs [58]. As illustrated in Fig. 7a, catheters covered with MRSA-induced biofilm were implanted into the back of mice. The mice were divided randomly into five groups (PBS+L, NPs, NPs+L, DA_3-NPS, DA_3-NPs+L), and the time was marked as day 0. Topical drug administration was conducted twice (3 mg/kg per time) on days 1–2. Phototherapy (808 nm, 0.33 W/cm^2, 10 min) was performed once on day 3, and the catheter was taken out on day 7 (Fig. 7b). The collected catheters were stained by CV dye. Compared with those in the other treatment groups, only the catheter in the DA_3-NPs+L group was clean, and no biofilms could be found on its surface (Fig. 7c). Statistical analysis displayed that biofilm mass in the DA_3-NPs+L group significantly decreased to 4 %, while that in the suboptimal group of NPs+L was as high as 72 % (Fig. 7d). CFU counting further demonstrated the bactericidal efficiency of the DA_3-NPs+L group was as high as 99.99 % (Fig. 7e). Additionally, after the treatment of DA_3-NPs, the mice rapidly recovered with notable weight increase, while those in the groups of PBS+L, NPs, DA_3-NPs and NPs+L groups showed a sustained weight loss (Fig. 7f). This implied that DA_3-NPs+L possessed excellent performance for eliminating implant biofilm *in vivo*.

Subsequently, the tissues around the implant infection were collected for staining analysis. Gram stain of the tissues showed that numerous bacteria with dark purple color (red arrows) appeared in the tissues of PBS+L, NPs, and DA_3-NPs groups (Fig. 7g). The NPs+L group also showed residual bacteria, but the number notably decreased. This implied that biofilm-based implant infection could allow bacteria to invade surrounding tissues. In contrast, no bacteria was observed in the tissue after the treatment of DA_3-NPs+L, suggesting DA_3-NPs+L could effectively kill bacteria within the biofilm, thereby inhibiting their diffusion. Consistently, the H&E stains results showed numerous inflammatory cell infiltrations (green arrows) in the groups of PBS+L, NPs, DA_3-NPs, and NPs+L, whereas the phenomenon was notably reduced in the DA_3-NPs+L group, suggesting DA_3-NPs+L could effectively relieve inflammation.

Immune regulation

It was reported that PDT or PTT could effectively activate immunity [59]. M1 macrophage is able to secret pro-inflammatory cytokines, such as tumor necrosis factor-α (TNF-α) and interleukin 6 (IL-6), to continuously induce inflammatory response [60]. However, biofilm infections inhibit the release of anti-inflammatory factors such as interleukin 10 (IL-10) and transforming growth factor-β (TGF-β) [61]. The homogeneous tissues around the implants were collected and analyzed by ELISA. The results showed that the expressions of the pro-inflammatory factors IL-6 and TNF-α were high, while the expressions of anti-inflammatory factors IL-10 and TGF-β were low in PBS+L, NPs, and DA_3-NPs groups (Fig. 8a). This was due to the presence of biofilms, which continuously induced M1 phenotype macrophages to release inflammatory factors. In contrast, the expression of anti-inflammatory factors were significantly elevated after NPs+L treatment. In the case of DA_3-NPs+L, the expression of IL-10 and TGF-β expression were significantly pronounced, indicating that PDT could effectively suppress the inflammatory response.

Additionally, macrophages in the surrounding tissues of the implant were investigated using immunofluorescence staining (Fig. 8b). The results showed that inflammatory cells infiltrating around biofilm implants could be labeled with F4/80 (a macrophage marker in yellow fluorescence), indicating that most inflammatory cells were macrophages. CD80 (an M1 marker in red fluorescence) and CD206 (an M2 marker in green fluorescence), as classical biomarkers of the pro-inflammatory M1 and anti-inflammatory M2 phenotypes of macrophages, were stained in the surrounding tissue of the implant [62]. For PBS+L, NPs, and DA_3-NPs groups, many M1 phenotype giant macrophages were observed, suggesting biofilms could promote the polarization of macrophage-like pro-inflammatory M1 phenotype, thereby inhibiting macrophage killing of bacteria and allowing bacteria within the biofilm to achieve immune escape. Comparatively, an increased proportion of M2 macrophages was observed in the NPs+L group. For the DA_3-NPs+L group, it was showed that the proportion of M2 macrophages notably increased. The fluorescence ratios of CD80 to CD206 indicated that the M2/M1 ratios in the groups of PBS+L, NPs, DA_3-NPs and NPs+L were 0.05, 0.11, 0.07, and 0.66, respectively (Fig. 8c). In contrast, that in the DA_3-NPs+L group exhibited a significantly higher ratio, which was up to 2.78, suggesting that DA_3-NPs+L could promote macrophage differentiation towards the M2 phenotype and suppressed inflammatory response, which was in favor of restoring the bactericidal

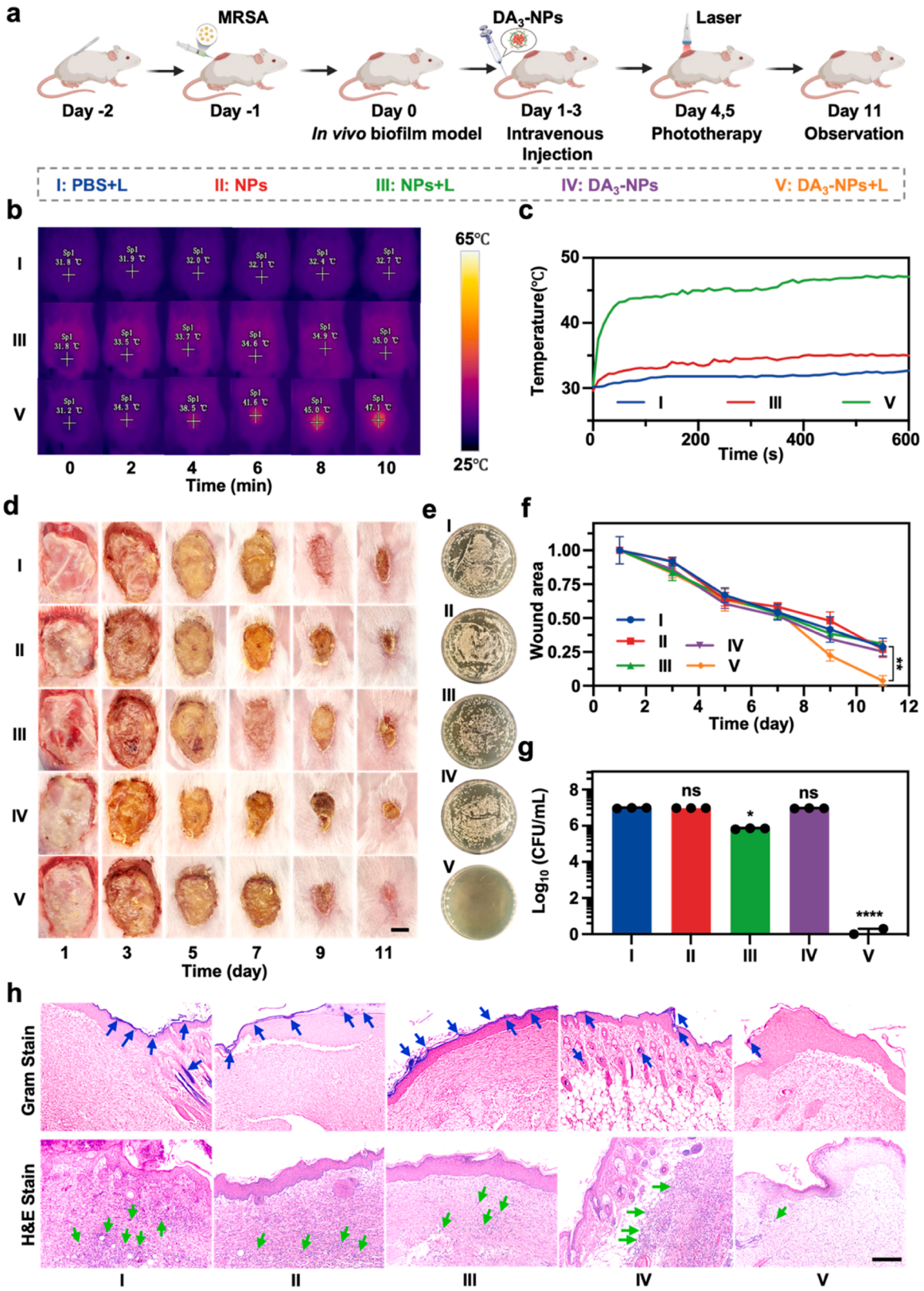

Fig. 6. *In vivo* biofilm elimination of DA_3-NPs and NPs in the biofilm-infection wound model. (a) Schematic illustration of the biofilm-infection wound infection model. (b) Thermographic images and (c) temperature changes in different treatment groups. (d) Photographs of the MRSA biofilm-infected wounds. Scale bar = 3 mm. (e) Photographs of bacterial colony plates after treatments. (f) Normalized wound area. (g) CFU counting of the infected wound on day 11. (h) Gram and H&E staining of the infected wounds. Scale bar = 200 μm. Laser irradiation conditions: 808 nm, 0.33 W/cm^2, 10 min. Data are expressed as the mean ± SD, Student's t-test, n = 3, ns $p>0.05$, * $p<0.05$, ** $p<0.01$, and **** $p<0.0001$.

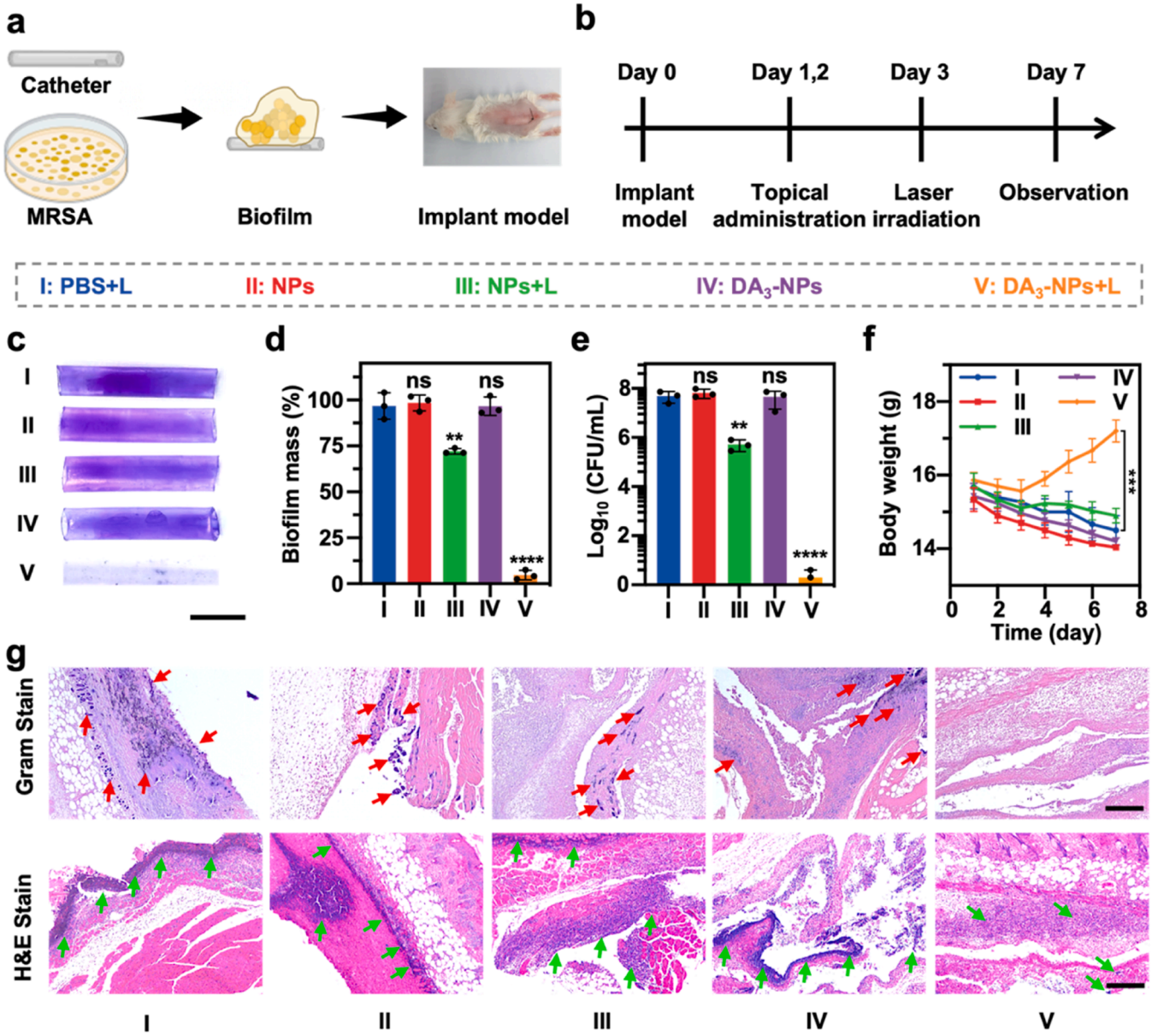

Fig. 7. *In vivo* biofilm elimination of DA_3-NPs and NPs in the catheter biofilm infection model. (a) Schematic illustration of the *in vivo* catheter biofilm infection model. (b) Timeline of the treatment process. (c) CV images of the implanted catheters. Scale bar = 1 mm. (d) Biofilm mass and (e) CFU counting of the implanted catheters at day 7. (f) Body weight changes. (g) Gram and H&E staining of peri-implant tissues at day 7. Scale bar = 200 μm. Data are expressed as the mean ± SD, Student's t-test, n = 3, ns $p>0.05$, ** $p<0.01$, *** $p<0.001$, and **** $p<0.0001$.

effect of macrophages.

Biosafety of DA_3-NPs

Finally, the biological safety of NPs and DA_3-NPs was evaluated. MTT assay showed that the nanoparticles (NPs & DA_3-NPs) were cellular compatible at wide-range dosages of < 100 μg/mL (Fig. S26A). Besides, *in vivo* safety evaluation showed that the mice after intravenous injection of the nanoparticles (5 mg/kg per time, injections every 2 days) exhibited continuous weight increase within 14 days (Fig. S26B). The blood biochemical indicators of the mice were similar to those of the untreated group, indicating that the drug administration did not affect the physiological health of the mice (Fig. S27). Additionally, H&E staining further confirmed that the primary organs (heart, liver, spleen, lung, and kidney) treated with the NPs and DA_3-NPs exhibited normal histomorphology without obvious pathological abnormalities (Fig. S28). The above results indicated that NPs and DA_3-NPs have the potential for clinical transformation.

Conclusions

We have developed a well-defined core-shell-shaped DA_3-NP *via* perfectly matched charge interaction. DA_3-NPs functioned robust abilities of EPS penetration and internal MRSA targeting because of the neutral potential and peptidoglycan anchor properties. Consequently, DA_3-NPs exerted precise *in-situ* phototherapy activity with appealing *in vitro* and *in vivo* eradication performances against MRSA-associated biofilm, which 61 times outperformed the non-targeting electronegative NPs. The DA_3-NPs had superior advantages: i) effective EPS penetration and precise internal MRSA targeting; ii) killing the MRSA within the biofilm by *in-situ* ROS release, carbon radicals and heat damage; iii) multiple stimuli responses, triggering shell-detachment and core-disintegration in a sequent manner, which was in favor of reinforcing anti-biofilm performance. iv) excellent biofilm eradication in the *in vivo*

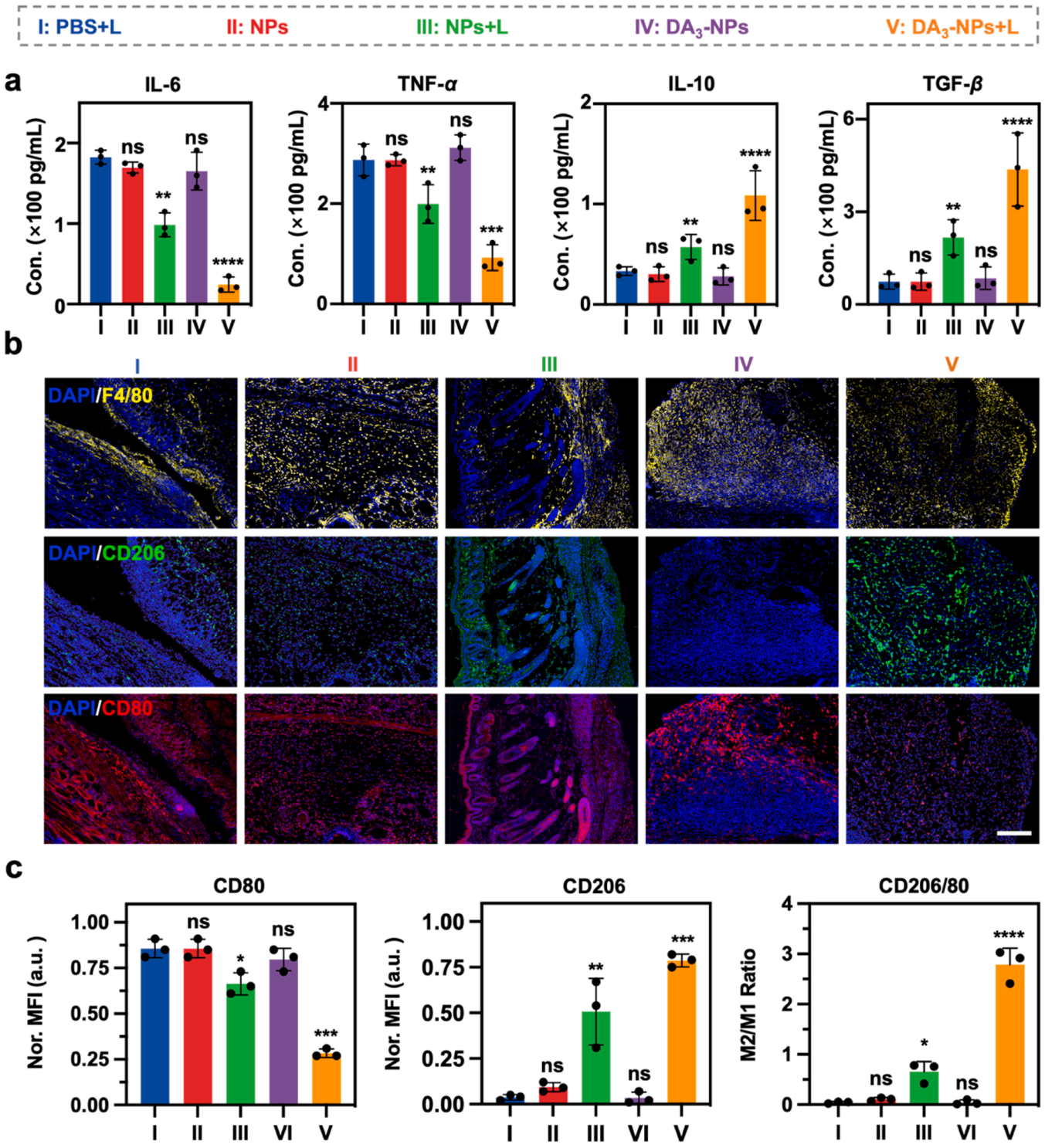

Fig. 8. Immune responses modulation of DA_3-NPs in catheter biofilm infection model. (a) Inflammatory (IL-6 and TNF-α) and anti-inflammatory (IL-10 and TGF-β) factors in the peri-implant tissues. (b) Immunofluorescence (F4/80, CD206, and CD80) of the peri-implant tissues. Scale bar = 100 μm. (c) The expression difference of CD80 (M1) and CD206 (M2) in different groups. Data are expressed as the mean ± SD, Student's t-test, n = 3, ns $p>0.05$, * $p<0.05$, ** $p<0.01$, *** $p<0.001$, and **** $p<0.0001$.

models of biofilm-infection wound and catheter biofilm infection. v) immune response remodel of the suppressed macrophages. Therefore, this study offers a precise *in-situ* phototherapy strategy for the nonantibiotic treatment of mature biofilm.

CRediT authorship contribution statement

Mengnan Liu: Methodology, Investigation, Conceptualization. **Wangtao Zhao:** Validation. **Fanqiang Bu:** Writing – original draft, Methodology, Investigation, Formal analysis, Data curation, Conceptualization. **Xing Wang:** Writing – review & editing, Supervision, Methodology, Funding acquisition, Conceptualization. **Wensheng Xie:**

Writing – review & editing, Supervision, Project administration. **Guofeng Li:** Writing – review & editing, Supervision, Funding acquisition, Conceptualization. **Fang Liu:** Validation, Methodology.

Declaration of Competing Interest

The authors declare that they have no known competing financial interests or personal relationships that could have appeared to influence the work reported in this paper.

Data availability

Data will be made available on request.

Acknowledgments

This work was supported by the National Natural Science Foundation of China (22275013, 52273118), the Fundamental Research Funds for the Central Universities (QNTD2023–01), and the Joint Project of BRC-BC (Biomedical Translational Engineering Research Center of BUCT-CJFH) (XK2023–16).

Research Support

This research received no external financial or non-financial support.

Relationships

There are no additional relationships to disclose.

Patents and Intellectual Property

There are no patents to disclose.

Other Activities

All authors have approved the current version. This manuscript has not been published elsewhere and is being submitted exclusively to Nano Today.

Appendix A. Supporting information

Supplementary data associated with this article can be found in the online version at doi:10.1016/j.nantod.2024.102449.

References

[1] O. Ciofu, C. Moser, P.Ø. Jensen, N. Høiby, Tolerance and resistance of microbial biofilms, Nat. Rev. Microbiol. 20 (2022) 621–635, https://doi.org/10.1038/s41579-022-00682-4.

[2] H. Koo, R.N. Allan, R.P. Howlin, P. Stoodley, L. Hall-Stoodley, Targeting microbial biofilms: current and prospective therapeutic strategies, Nat. Rev. Microbiol. 15 (2017) 740–755, https://doi.org/10.1038/nrmicro.2017.99.

[3] H. Zhang, Q. Chen, J. Xie, Z. Cong, C. Cao, W. Zhang, D. Zhang, S. Chen, J. Gu, S. Deng, Z. Qiao, X. Zhang, M. Li, Z. Lu, R. Liu, Switching from membrane disrupting to membrane crossing, an effective strategy in designing antibacterial polypeptide, Sci. Adv. 9 (2024) eabn0771, https://doi.org/10.1126/sciadv.abn0771.

[4] Z. Liu, K. Guo, L. Yan, K. Zhang, Y. Wang, X. Ding, N. Zhao, F.-J. Xu, Janus nanoparticles targeting extracellular polymeric substance achieve flexible elimination of drug-resistant biofilms, Nat. Commun. 14 (2023) 5132, https://doi.org/10.1038/s41467-023-40830-9.

[5] K. Sauer, P. Stoodley, D.M. Goeres, L. Hall-Stoodley, M. Burmølle, P.S. Stewart, T. Bjarnsholt, The biofilm life cycle: expanding the conceptual model of biofilm formation, Nat. Rev. Microbiol. 20 (2022) 608–620, https://doi.org/10.1038/s41579-022-00767-0.

[6] P. Tan, C. Wu, Q. Tang, T. Wang, C. Zhou, Y. Ding, H. Fu, S. Xu, Y. Feng, Y. Zhang, Q. Dai, X. Ma, pH-triggered size-transformable and bioactivity-switchable self-assembling chimeric peptide nanoassemblies for combating drug-resistant bacteria and biofilms, Adv. Mater. 35 (2023) 2210766, https://doi.org/10.1002/adma.202210766.

[7] D. Hu, Y. Deng, F. Jia, Q. Jin, J. Ji, Surface charge switchable supramolecular nanocarriers for nitric oxide synergistic photodynamic eradication of biofilms, ACS Nano 14 (2020) 347–359, https://doi.org/10.1021/acsnano.9b05493.

[8] A. Zhang, H. Wu, X. Chen, Z. Chen, Y. Pan, W. Qu, H. Hao, D. Chen, S. Xie, Targeting and arginine-driven synergizing photodynamic therapy with nutritional immunotherapy nanosystems for combating MRSA biofilms, Sci. Adv. 9 (2024) eadg9116, https://doi.org/10.1126/sciadv.adg9116.

[9] X. Liu, Y. Ren, D. Fan, S. Huang, Y. Ma, J. Ding, Z. Luo, F. Chen, W. Zeng, Shining light on multidrug-resistant bacterial infections: rational design of multifunctional organosilver-based aiegen probes as light-activated theranostics for combating biofilms and liver abscesses, Adv. Funct. Mater. 33 (2023) 2304974, https://doi.org/10.1002/adfm.202304974.

[10] Y. Zhan, X. Hu, Y. Li, Y. Wang, H. Chen, C.A. Omolo, T. Govender, H. Li, F. Huang, L. Shi, X. Hu, Y. Liu, Antimicrobial hybrid amphiphile via dynamic covalent bonds enables bacterial biofilm dispersal and bacteria eradication, Adv. Funct. Mater. 33 (2023) 2214299, https://doi.org/10.1002/adfm.202214299.

[11] X. Huang, L. Li, Z. Chen, H. Yu, X. You, N. Kong, W. Tao, X. Zhou, J. Huang, Nanomedicine for the detection and treatment of ocular bacterial infections, Adv. Mater. 35 (2023) 2302431, https://doi.org/10.1002/adma.202302431.

[12] X. Kang, F. Bu, W. Feng, F. Liu, X. Yang, H. Li, Y. Yu, G. Li, H. Xiao, X. Wang, Dual-cascade responsive nanoparticles enhance pancreatic cancer therapy by eliminating tumor-resident intracellular bacteria, Adv. Mater. 34 (2022) 2206765, https://doi.org/10.1002/adma.202206765.

[13] H. Zhang, Y. Zhu, Y. Li, X. Qi, J. Yang, H. Qi, Q. Li, Y. Ma, Y. Zhang, X. Zhang, L. Zhang, A bifunctional zwitterion-modified porphyrin for photodynamic nondestructive tooth whitening and biofilm eradication, Adv. Funct. Mater. 31 (2021) 2104799, https://doi.org/10.1002/adfm.202104799.

[14] W. Wang, Y. Hu, Z. Chen, L. Yu, S. Huang, Y. Zhang, J. Li, Y. Xue, A. Li, Y. Wang, Z. Wu, X. Zhang, Guanidine and galactose decorated nanophotosensitizer with oxygen self-sufficient capability for the localized ablation of oral biofilm, Adv. Funct. Mater. 33 (2023) 2300474, https://doi.org/10.1002/adfm.202300474.

[15] X. Han, Q. Lou, F. Feng, G. Xu, S. Hong, L. Yao, S. Qin, D. Wu, X. Ouyang, Z. Zhang, X. Wang, Spatiotemporal release of reactive oxygen species and no for overcoming biofilm heterogeneity, Angew. Chem., Int. Ed. 61 (2022) e202202559, https://doi.org/10.1002/anie.202202559.

[16] D. Yan, Y. Huang, J. Zhang, Q. Wu, G. Song, J. Ji, Q. Jin, D. Wang, B.Z. Tang, Adding flying wings: butterfly-shaped nir-ii aiegens with multiple molecular rotors for photothermal combating of bacterial biofilms, J. Am. Chem. Soc. 145 (2023) 25705–25715, https://doi.org/10.1021/jacs.3c09058.

[17] Y. Deng, Y. Fu, S.L. Chua, B.L. Khoo, Biofilm potentiates cancer-promoting effects of tumor-associated macrophages in a 3D multi-faceted tumor model, Small 19 (2023) 2205904, https://doi.org/10.1002/smll.202205904.

[18] J.-H. Yan, D.-W. Zheng, H.-Y. Gu, Y.-J. Yu, J.-Y. Zeng, Q.-W. Chen, A.-X. Yu, X.-Z. Zhang, In Situ sprayed biotherapeutic gel containing stable microbial communities for efficient anti-infection treatment, Adv. Sci. 10 (2023) 2205480, https://doi.org/10.1002/advs.202205480.

[19] L. Chen, M. Peng, J. Zhou, X. Hu, Y. Piao, H. Li, R. Hu, Y. Li, L. Shi, Y. Liu, Supramolecular photothermal cascade nano-reactor enables photothermal effect, cascade reaction, and in situ hydrogelation for biofilm-associated tooth-extraction wound healing, Adv. Mater. 35 (2023) 2301664, https://doi.org/10.1002/adma.202301664.

[20] V. Choi, J.L. Rohn, P. Stoodley, D. Carugo, E. Stride, Drug delivery strategies for antibiofilm therapy, Nat. Rev. Microbiol. 21 (2023) 555–572, https://doi.org/10.1038/s41579-023-00905-2.

[21] P. Prateeksha, V. Sharma, N. Nagpoore, V. Jadaun, C. Rao, B. Singh, Bacteria-responsive multidrug delivery nanosystem for combating long-term biofilm-associated infections, Adv. Funct. Mater. 33 (2023) 2214852, https://doi.org/10.1002/adfm.202214852.

[22] T. Wang, E.J. Cornel, C. Li, J. Du, Drug delivery approaches for enhanced antibiofilm therapy, J. Control. Release 353 (2023) 350–365, https://doi.org/10.1016/j.jconrel.2022.12.002.

[23] Y. Li, D. Li, J. Wang, T. Ye, Q. Li, L. Li, R. Gao, Y. Wang, J. Ren, F. Li, J. Lu, E. He, Y. Jiao, L. Wang, Y. Zhang, A temperature-sensing hydrogel coating on the medical catheter, Adv. Funct. Mater. 34 (2023) 2310260, https://doi.org/10.1002/adfm.202310260.

[24] Y. Wu, P. Liu, B. Mehrjou, P.K. Chu, Interdisciplinary-inspired smart antibacterial materials and their biomedical applications, Adv. Mater. 36 (2024) 2305940, https://doi.org/10.1002/adma.202305940.

[25] H. Douafer, V. Andrieu, J.M. Brunel, Scope and limitations on aerosol drug delivery for the treatment of infectious respiratory diseases, J. Control. Release 325 (2020) 276–292, https://doi.org/10.1016/j.jconrel.2020.07.002.

[26] J. Zhang, M. Liu, H. Guo, S. Gao, Y. Hu, G. Zeng, D. Yang, Nanotechnology-driven strategies to enhance the treatment of drug-resistant bacterial infections, Wires Nanomed. Nanobi. 16 (2024) e1968, https://doi.org/10.1002/wnan.1968.

[27] Y. Yu, Y. Zhang, Y. Cheng, Y. Wang, Z. Chen, H. Sun, X. Wei, Z. Ma, J. Li, Y. Bai, Z. Wu, X. Zhang, NIR-activated nanosystems with self-modulated bacteria targeting for enhanced biofilm eradication and caries prevention, Bioact. Mater. 13 (2022) 269–285, https://doi.org/10.1016/j.bioactmat.2021.10.035.

[28] R.T. Rozenbaum, O.C.J. Andrén, H.C. Van Der Mei, W. Woudstra, H.J. Busscher, M. Malkoch, P.K. Sharma, Penetration and accumulation of dendrons with different peripheral composition in pseudomonas aeruginosa biofilms, Nano Lett. 19 (2019) 4327–4333, https://doi.org/10.1021/acs.nanolett.9b00838.

[29] C. Song, W. Sun, Y. Xiao, X. Shi, Ultrasmall iron oxide nanoparticles: synthesis, surface modification, assembly, and biomedical applications, Drug Discov. Today 24 (2019) 835–844, https://doi.org/10.1016/j.drudis.2019.01.001.

[30] W. Feng, M. Chittò, W. Xie, Q. Ren, F. Liu, X. Kang, D. Zhao, G. Li, T.F. Moriarty, X. Wang, Poly(d-amino acid) nanoparticles target staphylococcal growth and biofilm disassembly by interfering with peptidoglycan synthesis, ACS Nano (2024) 8017–8027, https://doi.org/10.1021/acsnano.3c10983.
[31] H.J. Xiang, H.P. Tham, M.D. Nguyen, S.Z. Fiona Phua, W.Q. Lim, J.G. Liu, Y. Zhao, An Aza-BODIPY based near-infrared fluorescent probe for sensitive discrimination of cysteine/homocysteine and glutathione in living cells, Chem. Commun. 53 (2017) 5220–5223, https://doi.org/10.1039/c7cc01814b.
[32] H. Wang, T. Qin, W. Wang, X. Zhou, F. Lin, G. Liang, Z. Yang, Z. Chi, B.Z. Tang, Selenium-containing type-i organic photosensitizers with dual reactive oxygen species of superoxide and hydroxyl radicals as switch-hitter for photodynamic therapy, Adv. Sci. 10 (2023) 2301902, https://doi.org/10.1002/advs.202301902.
[33] Y. Li, D. Zhang, Y. Yu, L. Zhang, L. Li, L. Shi, G. Feng, B.Z. Tang, A cascade strategy boosting hydroxyl radical generation with aggregation-induced emission photosensitizers-albumin complex for photodynamic therapy, ACS Nano 17 (2023) 16993–17003, https://doi.org/10.1021/acsnano.3c04256.
[34] Z.-H. Xie, C.-S. He, D.-N. Pei, Y. Dong, S.-R. Yang, Z. Xiong, P. Zhou, Z.-C. Pan, G. Yao, B. Lai, Review of characteristics, generation pathways and detection methods of singlet oxygen generated in advanced oxidation processes (AOPs), Chem. Eng. J. 468 (2023) 143778, https://doi.org/10.1016/j.cej.2023.143778.
[35] Q.-Y. Li, Y.-H. Deng, C. Cao, Y.-X. Hong, X.-R. Xue, M.-J. Zhang, Y. Ge, B. F. Abrahams, J.-P. Lang, Visible light and microwave-mediated rapid trapping and release of singlet oxygen using a coordination polymer, Angew. Chem., Int. Ed. 62 (2023) e202306719, https://doi.org/10.1002/anie.202306719.
[36] W. Feng, G. Li, X. Kang, R. Wang, F. Liu, D. Zhao, H. Li, F. Bu, Y. Yu, T.F. Moriarty, Q. Ren, X. Wang, Cascade-targeting poly(amino acid) nanoparticles eliminate intracellular bacteria via on-site antibiotic delivery, Adv. Mater. 34 (2022) 2109789, https://doi.org/10.1002/adma.202109789.
[37] S. Li, L. Fu, X. Xiao, H. Geng, Q. Liao, Y. Liao, H. Fu, Regulation of thermally activated delayed fluorescence to room-temperature phosphorescent emission channels by controlling the excited-states dynamics via J- and H-aggregation, Angew. Chem., Int. Ed. 60 (2021) 18059–18064, https://doi.org/10.1002/anie.202103192.
[38] A.P. Senft, T.P. Dalton, H.G. Shertzer, Determining glutathione and glutathione disulfide using the fluorescence probe o-phthalaldehyde, Anal. Biochem. 280 (2000) 80–86, https://doi.org/10.1006/abio.2000.4498.
[39] X. Liu, Y. Yang, M. Ling, R. Sun, M. Zhu, J. Chen, M. Yu, Z. Peng, Z. Yu, X. Liu, Near-infrared ii light-triggered robust carbon radical generation for combined photothermal and thermodynamic therapy of hypoxic tumors, Adv. Funct. Mater. 31 (2021) 2101709, https://doi.org/10.1002/adfm.202101709.
[40] R.P. Rastogi, S.P. Singh, D.-P. Häder, R.P. Sinha, Detection of reactive oxygen species (ROS) by the oxidant-sensing probe 2′,7′-dichlorodihydrofluorescein diacetate in the cyanobacterium anabaena variabilis PCC 7937, Biochem. Biophys. Res. Commun. 397 (2010) 603–607, https://doi.org/10.1016/j.bbrc.2010.06.006.
[41] J. Hu, N. Liu, Q. Fan, Y. Gu, S. Chen, F. Zhu, Y. Cheng, A fluorous peptide amphiphile with potent antimicrobial activity for the treatment of MRSA-induced sepsis and chronic wound infection, Angew. Chem., Int. Ed. 63 (2024) e202403140, https://doi.org/10.1002/anie.202403140.
[42] B. Li, J. Mao, J. Wu, K. Mao, Y. Jia, F. Chen, J. Liu, Nano–bio interactions: biofilm-targeted antibacterial nanomaterials, Small 20 (2023) 2306135, https://doi.org/10.1002/smll.202306135.
[43] H. Wu, M. Wei, S. Hu, P. Cheng, S. Shi, F. Xia, L. Xu, L. Yin, G. Liang, F. Li, D. Ling, A photomodulable bacteriophage-spike nanozyme enables dually enhanced biofilm penetration and bacterial capture for photothermal-boosted catalytic therapy of MRSA infections, Adv. Sci. 10 (2023) 2301694, https://doi.org/10.1002/advs.202301694.
[44] X. Lv, L. Wang, A. Mei, Y. Xu, X. Ruan, W. Wang, J. Shao, D. Yang, X. Dong, Recent nanotechnologies to overcome the bacterial biofilm matrix barriers, Small 19 (2023) 2206220, https://doi.org/10.1002/smll.202206220.
[45] B. Zhang, S. Huang, L. Wu, Y. Guo, W. Shi, P.N.L. Lens, Micro(nano)plastic size and concentration co-differentiate the treatment performance and toxicity mechanism in aerobic granular sludge systems, Chem. Eng. J. 457 (2023) 141212, https://doi.org/10.1016/j.cej.2022.141212.
[46] X. Lv, J. Jiang, J. Ren, H. Li, D. Yang, X. Song, Y. Hu, W. Wang, X. Dong, Nitric oxide-assisted photodynamic therapy for enhanced penetration and hypoxic bacterial biofilm elimination, Adv. Healthc. Mater. 12 (2023) 2302031, https://doi.org/10.1002/adhm.202302031.
[47] Y. Liu, L. Shi, L. Su, H.C. Van der Mei, P.C. Jutte, Y. Ren, H.J. Busscher, Nanotechnology-based antimicrobials and delivery systems for biofilm-infection control, Chem. Soc. Rev. 48 (2019) 428, https://doi.org/10.1039/c7cs00807d.
[48] C.R. Thorn, C. de S. Carvalho-Wodarz, J.C. Horstmann, C.-M. Lehr, C.A. Prestidge, N. Thomas, Tobramycin liquid crystal nanoparticles eradicate cystic fibrosis-related pseudomonas aeruginosa biofilms, Small 17 (2021) 2100531, https://doi.org/10.1002/smll.202100531.
[49] P. Ren, T. Chen, N. Liu, W. Sun, G. Hu, Y. Yu, B. Yu, P. Ouyang, D. Liu, Y. Chen, Efficient biofilm-based fermentation strategies by eDNA formation for l-proline production with corynebacterium glutamicum, ACS Omega 5 (2020) 33314–33322, https://doi.org/10.1021/acsomega.0c05095.
[50] Y. Xu, Y. Luo, Z. Weng, H. Xu, W. Zhang, Q. Li, H. Liu, L. Liu, Y. Wang, X. Liu, L. Liao, X. Wang, Microenvironment-responsive metal-phenolic nanozyme release platform with antibacterial, ROS scavenging, and osteogenesis for periodontitis, ACS Nano 17 (2023) 18732–18746, https://doi.org/10.1021/acsnano.3c01940.
[51] A.J. McBain, Chapter 4 In Vitro biofilm models: an overview, Adv. Appl. Microbiol. 69 (2009) 99–132, https://doi.org/10.1016/S0065-2164(09)69004-3.
[52] A.K. Seth, M.R. Geringer, S.J. Hong, K.P. Leung, T.A. Mustoe, R.D. Galiano, In Vivo modeling of biofilm-infected wounds: a review, J. Surg. Res. 178 (2012) 330–338, https://doi.org/10.1016/j.jss.2012.06.048.
[53] K. Yang, D. Liu, R. Teng, C. Li, Z. Fan, J. Du, An antibacterial polypeptide coating prepared by in situ enzymatic polymerization for preventing delayed infection of implants, ACS Biomater. Sci. Eng. 9 (2023) 1900–1908, https://doi.org/10.1021/acsbiomaterials.3c00131.
[54] Y. Wang, L.I. Cheng, D.R. Helfer, A.G. Ashbaugh, R.J. Miller, A.J. Tzomides, J. M. Thompson, R.V. Ortines, A.S. Tsai, H. Liu, C.A. Dillen, N.K. Archer, T.S. Cohen, C. Tkaczyk, C.K. Stover, B.R. Sellman, L.S. Miller, Mouse model of hematogenous implant-related staphylococcus aureus biofilm infection reveals therapeutic targets, Proc. Natl. Acad. Sci. U. S. A. 114 (2017) E5094–E5102, https://doi.org/10.1073/pnas.1703427114.
[55] D. Pranantyo, C.K. Yeo, Y. Wu, C. Fan, X. Xu, Y.S. Yip, M.I.G. Vos, S. H. Mahadevegowda, P.L.K. Lim, L. Yang, P.T. Hammond, D.I. Leavesley, N.S. Tan, M.B. Chan-Park, Hydrogel dressings with intrinsic antibiofilm and antioxidative dual functionalities accelerate infected diabetic wound healing, Nat. Commun. 15 (2024) 954, https://doi.org/10.1038/s41467-024-44968-y.
[56] F. Bu, X. Kang, D. Tang, F. Liu, L. Chen, P. Zhang, W. Feng, Y. Yu, G. Li, H. Xiao, X. Wang, Enhancing near-infrared ii photodynamic therapy with nitric oxide for eradicating multidrug-resistant biofilms in deep tissues, Bioact. Mater. 33 (2024) 341–354, https://doi.org/10.1016/j.bioactmat.2023.11.006.
[57] G. Jiang, R. Wu, S. Liu, T. Yu, Y. Ren, H.J. Busscher, H.C. van der Mei, J. Liu, Ciprofloxacin-loaded, pH-responsive PAMAM-megamers functionalized with s-nitrosylated hyaluronic acid support infected wound healing in mice without inducing antibiotic resistance, Adv. Healthc. Mater. 13 (2024) 2301747, https://doi.org/10.1002/adhm.202301747.
[58] M. Verma, A. Nisha, M. Bathla, A. Acharya, Resveratrol-encapsulated glutathione-modified robust mesoporous silica nanoparticles as an antibacterial and antibiofilm coating agent for medical devices, ACS Appl. Mater. Interfaces 15 (2023) 58212–58229, https://doi.org/10.1021/acsami.3c13733.
[59] Y. Lu, W. Sun, J. Du, J. Fan, X. Peng, Immuno-photodynamic therapy (IPDT): organic photosensitizers and their application in cancer ablation, JACS Au 3 (2023) 682–699, https://doi.org/10.1021/jacsau.2c00591.
[60] A. Taglialegna, A killer biofilm, Nat. Rev. Microbiol. 21 (2023) 484, https://doi.org/10.1038/s41579-023-00928-9.
[61] C. Mao, W. Jin, Y. Xiang, Y. Zhu, J. Wu, X. Liu, S. Wu, Y. Zheng, K.M.C. Cheung, K. W.K. Yeung, Realizing highly efficient sonodynamic bactericidal capability through the phonon–electron coupling effect using two-dimensional catalytic planar defects, Adv. Mater. 35 (2023) 2208681, https://doi.org/10.1002/adma.202208681.
[62] X. Bao, B. Liu, Y. Jiang, T. Feng, W. Cao, J. Shi, Y. Jiang, X. Chen, J. Yang, J. Li, Z. Zhou, Loss of SENP3 mediated the formation of nasal polyps in nasal mucosal inflammation by increasing alternative activated macrophage, Immun. Inflamm. Dis. 11 (2023) e781, https://doi.org/10.1002/iid3.781.